nature nanotechnology

Article

https://doi.org/10.1038/s41565-025-01898-0

Li^+(ionophore) nanoclusters engineered aqueous/non-aqueous biphasic electrolyte solutions for high-potential lithium-based batteries

Received: 25 July 2023

Accepted: 28 February 2025

Published online: 08 April 2025

Check for updates

Xiyue Zhang[1], Travis P. Pollard[2], Sha Tan[3], Nan Zhang[1], Jijian Xu[1], Yijie Liu[1], An L. Phan[1], Weiran Zhang[4], Fu Chen[5], Chongyin Yang[6], Enyuan Hu[3], Xiao-Qing Yang[3], Oleg Borodin[2] ✉ & Chunsheng Wang[1] ✉

The use of aqueous/non-aqueous biphasic electrolyte solutions in Li-based battery systems circumvents the limitations of poor reductive stability of aqueous electrolyte solutions, broadening their electrochemical stability window. However, aqueous/non-aqueous electrolytes suffer from biphasic mixing and high impedance when Li ions cross the biphasic interface. Here we propose the use of 12-crown-4 (12C4) and tetraglyme (G4) as lithium ionophores to form Li^+(ionophore) nanoclusters in both non-aqueous and aqueous phases to overcome the interface challenges in biphasic electrolytes. The Li^+(ionophore) nanoclusters have the H_2O-excluding inner Li^+ solvation structure in non-polar 1,1,2,2-tetrafluoroethyl 2,2,3,3-tetrafluoropropyl ether (TTE), allowing fast charge transport across the biphasic interface without solvent mixing or water shuttling. A tailored electrolyte formulation comprising the lithium bis(trifluoromethanesulfonyl)imide (LiTFSI) salt, 12C4, TTE and H_2O solvents (labelled LiTFSI–12C4@TTE/H_2O) demonstrates low impedance (2.7 Ω cm^{-2}) at the TTE/H_2O interface and enabling 2,000 cycles of prelithiated graphite||$LiFePO_4$ coin cells at 850 mA g^{-1} with an average Coulombic efficiency of 99.8%. Single-layer 22.5 mAh Li||$LiMn_2O_4$ pouch cells using LiTFSI–12C4@TTE/H_2O electrolyte with G4 delivered a stable discharge capacity of about 1.3 mAh cm^{-2} for 80 cycles at 0.5 mA cm^{-2}.

Meeting the demand for portable electronics, electric vehicles and large-scale grid storage requires Li-ion batteries (LIBs) with high energy content and improved safety, which are challenging for state-of-the-art organic-based non-aqueous LIB electrolyte solutions. Aqueous LIBs are safer than their non-aqueous counterpart but possess lower energy density owing to the narrowed electrochemical stability window (ESW) of aqueous electrolytes. Highly concentrated water-in-salt (WiS) electrolyte solutions extend the range of ESWs from 1.23 V to 3.0 V through the formation of a LiF-rich solid electrolyte interphase (SEI) on the negative electrode and adsorption of hydrophobic anion at the positive electrode. The oxidative limiting potential of WiS reaches 4.9 V (versus $Li|Li^+$), which is higher than that of some carbonate-based non-aqueous electrolyte solutions (that is, 4.2 V versus $Li|Li^+$)[1,2]. However, unlike organic electrolytes, WiS electrolytes generate gas upon reduction at 1.9 V versus $Li|Li^+$, inhibiting the reversible operation of graphite and lithium metal negative electrodes[1]. Efforts have been made to extend

A full list of affiliations appears at the end of the paper. ✉e-mail: oleg.a.borodin.civ@army.mil; cswang@umd.edu

https://doi.org/10.1038/s41565-025-01898-0

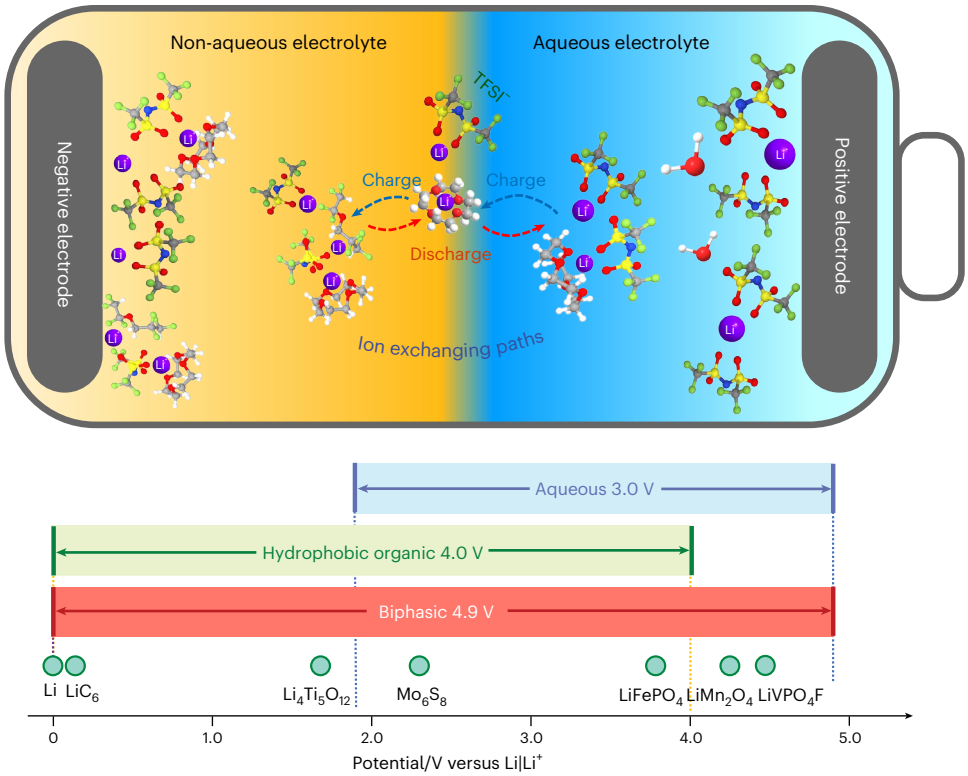

Fig. 1 | Lithium ionophore biphasic electrolyte design strategy. Schematic illustrations of the (top) lithium ionophore (for example, 12C4) nanoclusters engineered biphasic electrolyte for Li-based batteries and (bottom) ESWs of aqueous, non-aqueous organic, biphasic electrolytes, and the theoretical working potentials of various negative and positive battery electrode active materials. Atom colour legend in the upper part of the figure: purple (Li); green (F); red (O); white (H); yellow (S); blue (N); and grey (C).

the limited reductive stability of aqueous electrolytes by adding organic additives, including poly(ethylene glycol)[3], dimethyl sulfoxide (DMSO)[4] and urea [$CO(NH_2)_2$][5], which dissolve in the electrolyte and modify the Li^+ solvation shell, reducing water and forming a nanocomposite inorganic–organic SEI. However, the lowest reductive potential limit achieved so far is only 1.3 V versus Li|Li^+ (ref. 3).

A biphasic electrolyte design is attractive for extending the reductive limiting potential of aqueous electrolytes and, thus, the ESW[6]. However, achieving high Li^+ transport in both phases and across the interface without water shuttling remains an unsolved challenge. Two basic strategies exist for forming biphasic electrolytes, one using a membrane to physically separate the two media and the other by combining two immiscible phases. Solid ion-conducting membranes, such as ceramic films[7,8], metal–organic frameworks[9] or functionalized polymers[10,11], suffer from fragility, low ionic conductivity and high cost[12]. Ruptures or manufacturing defects pose safety risks[13], while their reactions with liquid electrolytes induce additional SEI formation, increasing interfacial impedance[14].

For self-phase-separated electrolytes formed using immiscible aqueous and non-aqueous solvents[15,16], highly fluorinated ethers, such as 1,1,2,2-tetrafluoroethyl 2,2,3,3-tetrafluoropropyl ether (TTE), are preferred organic solvents owing to their strong phase separation from aqueous electrolytes. However, Li^+ conductivity and Li-salt solubility in TTE are inadequate for battery applications. The use of dimethyl carbonate (DMC) as an additive to TTE can increase the solubility of Li salts[6]. However, water also penetrates the TTE–DMC phase since H_2O easily replaces DMC in the Li^+ first solvation shell owing to stronger $Li^+(H_2O)_n$ solvation than $Li^+(DMC)_m$, leading to low Coulombic efficiency (CE) and poor durability for Li||$LiFePO_4$ coin cells[6].

Fast ion transfer between two immiscible liquid phases is reported in living organisms[17]. Different ionophores selectively bind cations, enabling rapid and efficient ion transfer between the aqueous and organic phases[18]. Here we design and characterize a series of lithium ionophore-enabled biphasic electrolytes that lower interface impedance while preventing H_2O and organic solvent mixing during Li^+ transport (Fig. 1). The biphasic electrolytes are prepared using 12-crown-4 ether (12C4) and/or tetraglyme (G4) as ionophores, lithium bis(trifluoromethanesulfonyl)imide (LiTFSI) as salt, combined with TTE non-aqueous liquid and water-in-bisalt (WiBS) aqueous electrolytes, forming a clear interface (Supplementary Fig. 1). The 0.5 M $Li_{1.1}$(12C4)$TFSI_{1.1}$–TTE/0.8 M Li(12C4)TFSI–WiBS biphasic electrolyte (denoted as LiTFSI–12C4@TTE/H_2O) has an ESW spanning from 0.0 V to 4.9 V versus Li|Li^+ with low water content in the organic phase (<200 ppm; Supplementary Fig. 2; <2 ppm when the aqueous phase is gelled with a hydrophilic polymer; Supplementary Figs. 3 and 4). The low water content in the organic phase is the result of water exclusion from the solvation shell of Li^+ cations that are coordinated either by 12C4 ionophores or $TFSI^-$ anions, which form contact ion pairs (CIPs) and charged aggregates (AGGs). These nanoclusters enable adequate bulk and interfacial ion transport with a low interface impedance of 2.7 Ω cm^{-2}. Moreover, AGGs in the organic phase facilitate LiF-rich SEI formation, enabling a high CE and cycle life in coin cells with prelithiated graphite-based or Li metal negative electrodes and $LiFePO_4$ (LFP) or $LiMn_2O_4$ (LMO) positive electrodes. The biphasic electrolyte tested in Li(20 μm)||$LiVPO_4F$(1.2 mAh cm^{-2}) coin cells enables a cell discharge capacity retention of 85.7% and an average CE of 99.4% after 100 cycles at 78 mA g^{-1} with an applied upper cut-off potential of 4.5 V.

Results and discussion

Principles of lithium ionophore biphasic electrolyte solutions design

Effective biphasic electrolyte solutions for battery applications should demonstrate (1) a large polarity difference between the organic solvent and the aqueous phase to ensure low solubility of water in the

https://doi.org/10.1038/s41565-025-01898-0

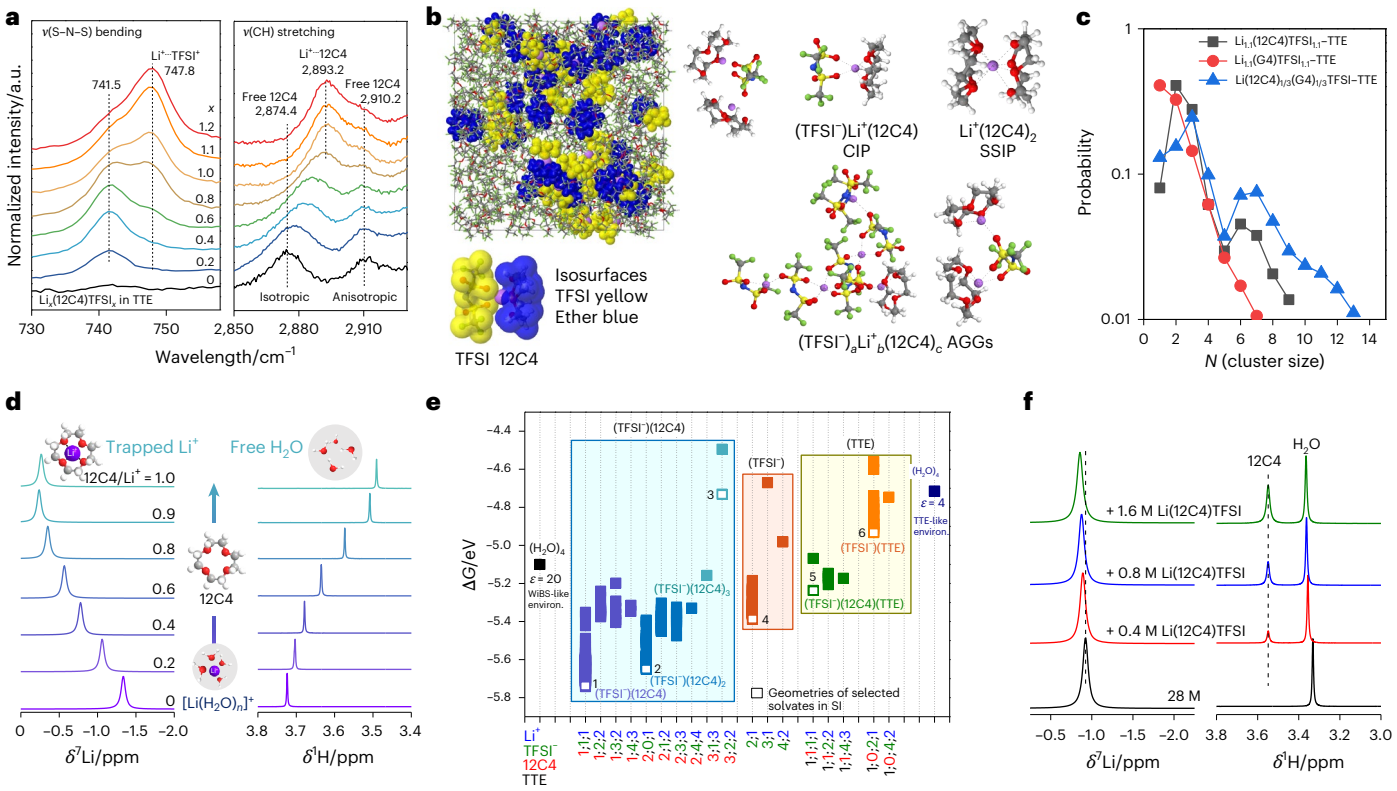

Fig. 2 | Solvation structure of biphasic electrolytes. a, The Raman spectra (at a temperature of 25 ± 0.05 °C) corresponding to the S–N–S bending vibration of $TFSI^-$ (left) and CH stretching vibration (right) of 12C4 in $Li_x(12C4)TFSI_x$–TTE electrolyte for various LiTFSI:12C4 molar ratios x. **b**, A snapshot of MD simulations box of $Li_{1.1}(12C4)TFSI_{1.1}$–TTE electrolyte highlighting $TFSI^-$ with a yellow isosurface, 12C4 with a blue isosurface, while TTE is shown as sticks. Representative solvates extracted from MD simulations are shown on the right. **c**, The probability of an ion to be a part of an ionic nanocluster of size N from MD simulations, $N = 0$ (free ions), $N = 1$ CIPs, $N \geq 2$ AGGs. **d**, The ^7Li (left) and ^1H (right) NMR chemical shifts of 0.55 M LiTFSI/TTE–acetonitrile(AN)–H_2O (TTE:AN = 7:3 in weight, H_2O = 10,000 ppm) solution at different 12C4:Li^+ molar ratios. **e**, Binding free energies (ΔG) of the $(TFSI^-)_a(Li^+)_b(12C4)_c(TTE)_d$ solvates immersed in an implicit solvent (SMD(ether)) relative to Li^+ in gas-phase and isolated solvents/anions in implicit solvent (Supplementary Note 8). Solvates are highlighted by whether they contain 12C4 (blue), only anions (red), 12C4 in TTE (green scatter in the yellow region) and anions in TTE (orange scatter in the yellow region). The corresponding solvate binding energies (ΔE) are shown in Supplementary Fig. 10. Geometries of the representative solvates (1–6) are shown in Supplementary Fig. 11. **f**, The ^7Li (left) and ^1H (right) NMR chemical shifts of WiBS aqueous electrolytes containing different concentrations of Li(12C4)TFSI complex.

non-aqueous electrolyte, (2) high salt solubility in both phases to maximize ionic conductivity in both aqueous and non-aqueous electrolytes, (3) solvent immiscibility and (4) low interfacial impedance (that is, <10 Ω cm^{-2}) for transporting Li^+ across the interface.

In this work, we selected TTE as a non-polar organic solvent owing to its high hydrophobicity, non-flammability and high electro-/chemical stability. To increase the solubility of Li salt in TTE while suppressing water solubility and shuttling, 12C4 with a cavity size complementary to Li^+ cations is used as an ionophore to exclude H_2O from the Li^+ first solvation shell. $(TFSI^-)_a(Li^+)_b(12C4)_c$ nanoclusters (a, b, c; Supplementary Note 1) can be dissolved in both TTE and H_2O solvents and shuttle Li^+ within and between the aqueous and organic phases. The aqueous phase that we used is a 28 m (molal) WiBS electrolyte solution comprising 21 m LiTFSI and 7 m lithium trifluoromethanesulfonate (LiOTF) salt[19]. Li(12C4)TFSI complex (0.8 M) was added to the WiBS electrolyte to balance the ionophore concentration between the two phases.

Solvation structure of biphasic electrolytes

The solvation structure of the organic and aqueous electrolyte phases of the biphasic electrolyte was investigated by Raman spectroscopy (Fig. 2a). Increasing Li^+:12C4 molar ratio x (Supplementary Note 2) resulted in the increase of 747.8 cm^{-1} S–N–S $TFSI^-$ band attributed to CIPs and AGGs, while the disappearance of 741.5 cm^{-1} band attributed to the loss of free $TFSI^-$ anions. Simultaneously, the fraction of free 12C4 (uncoordinated by Li^+) at 2,874 cm^{-1} and 2,910 cm^{-1} in C–H stretching vibration decreases to the point that no free 12C4 can be detected when $x \geq 1$. To minimize free 12C4, increase salt concentration but avoid electrolyte precipitation during battery cycling, the 0.5 M $Li_{1.1}(12C4)TFSI_{1.1}$–TTE electrolyte (denoted as LiTFSI–12C4@TTE) was selected, maintaining a composition slightly below the solubility limit $x = 1.2$ (Supplementary Fig. 5). Molecular dynamics (MD) simulations of the LiTFSI–12C4@TTE electrolyte (Supplementary Note 3 and Supplementary Fig. 6) demonstrate that the negatively charged AGGs and CIPs tend to be anchored by Li^+(12C4) and accumulate into larger clusters surrounded by TTE (Fig. 2b) with a significant probability of the ion clusters $N = 3$ (N, cluster size, the number of Li^+ plus the number of $TFSI^-$) that contribute to vehicular charge transport (black line in Fig. 2c and Supplementary Note 4) via Li^+/$TFSI^-$ charge aggregate diffusion (Supplementary Note 5). The pair distribution functions (PDF) and X-ray measurements (Supplementary Note 6 and Supplementary Figs. 7 and 8) further confirmed the solvation structure.

The $Li^+(12C4)_2$ and $Li^+(H_2O)_4$ solvation is compared by probing the relative strength of donor–acceptor interactions between Li^+–12C4 and Li^+–H_2O using ^7Li and ^1H nuclear magnetic resonance (NMR) spectroscopy (Fig. 2d). As the 12C4:Li^+ molar ratio increases closer to 1 in the water-containing solution, the chemical shift for ^7Li shifts downfield (higher chemical shift), indicating a change of the Li^+ solvation shell from H_2O to the crown ether[20,21]. The opposite trend was found for the ^1H signal from H_2O with an upfield chemical shift, demonstrating a

greater electron density. Therefore, free water molecules are released when adding 12C4 into the moisture-spiked electrolyte following the reaction:

$$[Li(H_2O)_n]^+ + (12C4)_m \rightarrow [Li(12C4)_m]^+ + nH_2O_{free}.$$

The stronger bonding of Li^+–12C4 than that of Li^+–H_2O was also confirmed by Raman spectroscopy (Supplementary Fig. 9 and Supplementary Note 7). Density functional theory (DFT) calculations confirmed that the $(TFSI^-)_aLi^+_b(12C4)_c$ solvates exhibit higher (more negative) binding energy and free energy than $Li^+(H_2O)_4$ hydrates (Fig. 2e, Supplementary Fig. 10 and Supplementary Note 8), following the order $(TFSI^-)(Li^+)(12C4)$ CIPs > $(Li^+)(12C4)_2$ solvent-separated ion pairs (SSIPs) > $(TFSI^-)_2(Li^+)(12C4)$ > $(TFSI^-)_2(Li^+)$ >> $Li^+(H_2O)_4$. In LiTFSI–12C4@TTE organic electrolytes, 12C4 strongly binds to Li^+, forming either $Li^+(12C4)_2$ SSIPs or $(TFSI^-)Li^+(12C4)$ CIPs and $(TFSI^-)_aLi^+_b(12C4)_c$ AGGs with multiple $TFSI^-$ complexing Li^+ (Supplementary Fig. 11), in accord with Li^+ coordination environments from MD simulations (Supplementary Table 1).

In aqueous WiBS electrolyte, with increasing concentration of Li(12C4)TFSI complex, the NMR chemical shifts for ^7Li and ^1H signal from H_2O shifted slightly downfield (Fig. 2f), indicating that a fraction of Li^+ is strongly bonded to 12C4 while other Li^+ are coordinated to H_2O. The unperturbed solvation structure of WiBS with the presence of Li(12C4)TFSI is confirmed using Fourier transform infrared spectroscopy (Supplementary Fig. 12) and PDF (Supplementary Fig. 7 and Supplementary Note 9).

Electrochemical properties of biphasic electrolytes

In LiTFSI–12C4@TTE electrolyte, MD simulations suggested the Li^+ transport occur via a vehicular transport mechanism through SSIPs and charged AGGs (Supplementary Table 1, Supplementary Notes 4 and 5). Thus, increasing SSIP by raising the salt concentration (green columns in Fig. 3a) and enhancing AGG charge carriers by adjusting the Li^+:12C4 ratio (x) leads to increased ionic conductivity in $Li_x(12C4)TFSI_x$–TTE organic electrolytes. The $Li_x(12C4)TFSI_x$–TTE electrolytes with Li^+ concentration of 0.55M and $x = 1.1$ reaches the highest bulk Li^+ conductivity (0.58 mS cm^{-1}, 25 ± 0.05 °C). The charged AGGs also facilitate charge transfer at the electrode interface (Supplementary Fig. 13 and Supplementary Note 10) owing to the faster exchange between Li^+ and $TFSI^-$ within the (12C4)-anchored AGGs than from 12C4.

In bulk WiBS aqueous electrolyte, increasing the Li(12C4)TFSI concentration (y; $0 \le y \le 1.6$) raises kinematic viscosity, thereby slightly reducing Li^+ transport (Fig. 3b and Supplementary Fig. 14). However, at the TTE/H_2O interface, as y increases from 0 to 1.6, the ion transport impedance decreases from 116.55 Ω cm^{-2} to 0.62 Ω cm^{-2} (Fig. 3c and Supplementary Fig. 15). The decreased interfacial impedance demonstrates the improved Li^+ transport across the biphasic interface owing to the charged transport by triplet charged AGGs that exhibit a faster Li^+–$TFSI^-$ exchange compared with Li^+–12C4. In addition, the reduced hydrophilicity of $(TFSI^-)_aLi^+_b(12C4)_c$ AGGs allows AGGs to exhibit similar affinities in either TTE or H_2O phase, thereby reducing the Li^+ migration impedance at the aqueous/non-aqueous interface. Importantly, owing to the dominance of ionic pairs and aggregates, ionic motion is highly correlated, as indicated by an inverse Haven ratio (also called ionicity)[22] of 0.15 (Supplementary Table 1 and Supplementary Note 11).

The ESW of the LiTFSI–12C4@TTE/H_2O biphasic electrolytes was evaluated to be 0.0–4.9 V versus Li|Li^+ via linear sweep voltammetry and cyclic voltammetry (CV) applying a scan rate of 1 mV s^{-1} and a temperature of 25 ± 0.05 °C (Fig. 3d). The Li^+-coordinated ether-based ionophores in WiSB do not impact the oxidative limit potential of 0.8 M Li(12C4)TFSI–WiBS electrolytes (Supplementary Fig. 16), owing to the rapid Li^+–$TFSI^-$ exchange in WiBS compared with Li^+(12C4). In the organic phase, the Li plating/stripping peak current in Li||Li symmetric cells increased 4 times as the Li^+:12C4 ratio x rose from 0.9 to 1.1 (Supplementary Fig. 17 and Supplementary Note 12). When $x = 1.1$, the slight reduction of $TFSI^-$ and TTE (Supplementary Fig. 18) led to the formation of a lithiophobic, LiF-rich SEI, thus achieving an average CE of 98.45% for the Li||Li cell (Supplementary Fig. 19) and an average CE of 99.54% for the Li||graphite cell (Supplementary Fig. 20) without ether co-intercalation (Supplementary Fig. 21). This LiF-rich SEI remains unchanged in the biphasic electrolyte as confirmed by X-ray photoelectron spectroscopy (XPS) (Supplementary Fig. 22 and Supplementary Note 13).

The effect of the y M Li(12C4)TFSI in the WiBS aqueous phase of biphasic electrolytes was evaluated in Li(20 μm, organic phase)||LFP (0.1 mAh cm^{-2}, aqueous phase) coin cells with the aqueous phase gelled by a hydrophilic polymer (Methods and Supplementary Fig. 23). When y is increased until $y = 0.8$, the discharge capacity of gelled Li||LFP cells increases (Supplementary Fig. 24). Once y reaches 1.6, the overpotential increases, and discharge capacity decreases (Supplementary Fig. 24) owing to the high viscosity of the aqueous electrolyte (Fig. 3b). The 0.8 M Li(12C4)TFSI–WiBS aqueous electrolyte (denoted as LiTFSI–12C4@WiBS) enables high cycling stability for both the Li||LFP (Supplementary Fig. 24) and graphite||LFP coin cells (Supplementary Fig. 25). When using LMO-based positive electrodes, which require high potentials up to 4.3 V versus Li|Li^+ and are incompatible with LiTFSI–12C4@TTE organic electrolytes (Supplementary Fig. 26), the biphasic LiTFSI–12C4@TTE/H_2O electrolyte, combining LiTFSI–12C4@TTE and LiTFSI–12C4@WiBS, enables reversible cycling of Li||LMO coin cells with high CE and rate capability (Supplementary Fig. 27).

Testing of the LiTFSI–12C4@TTE/H_2O biphasic electrolyte solution in various Li-based battery cell configurations

To highlight the critical role of 12C4 in the biphasic electrolyte, two control biphasic electrolytes (Supplementary Note 14), where 12C4 in LiTFSI–12C4@TTE/H_2O was replaced with DMC or DME, were evaluated. Even with an N/P ratio of ~40 and low LFP loading (0.1 mAh cm^{-2}), Li(20 μm)||LFP coin cells in DME- and DMC-based biphasic electrolytes exhibited rapid discharge capacity decay (Supplementary Note 15). By contrast, 72.3% discharge capacity retained after 930 cycles in LiTFSI–12C4@TTE/H_2O biphasic electrolytes (Fig. 4a,b and Supplementary Fig. 28) at 85 mA g^{-1}, with an average CE of ~99.8% at 25 ± 0.05 °C, similar to the performance in LiTFSI–12C4@TTE organic electrolytes (black dots), which retained 83.4% capacity after 1,050 cycles at 85 mA g^{-1}, with an average CE of ~99.94% at 25 ± 0.05 °C. When water-miscible 1 M lithium hexafluorophosphate ($LiPF_6$) in ethylene carbonate–ethyl methyl carbonate organic electrolyte is paired with the gelled WiBS aqueous electrolyte, the assembled Li(20 μm)||LFP(0.1 mAh cm^{-2}) battery cannot even complete one cycle (Supplementary Fig. 29).

The morphology of Li metal electrodes after cycling was investigated ex situ via scanning electron microscopy (SEM). The Li metal electrodes cycled in the Li||LFP coin cells in LiTFSI–12C4@TTE/H_2O biphasic electrolyte show a smooth surface with a dense morphology without dendritic structures after 200 cycles at 85 mA g^{-1} (Supplementary Fig. 30), while a rough surface of the Li metal electrode with Cu current collector exposure was observed in DME- and DMC-based biphasic electrolyte owing to the water contamination.

The Li(20 μm)||LFP(0.1 mAh cm^{-2}) coin cells exhibit similar rate performance in the biphasic electrolyte (Supplementary Fig. 31) as in the single organic electrolyte (Supplementary Fig. 32). The prelithiated(preLi)-graphite|LiTFSI–12C4@TTE/H_2O|LFP(0.1 mAh cm^{-2}) coin cells (Methods and Supplementary Fig. 33) demonstrated extended cycling life (Fig. 4c) and enhanced rate capability (Fig. 4d), retaining 65.1 mAh g^{-1} capacity at 850 mA g^{-1} after 2,000 cycles, with an average CE of ~99.8% at 25 ± 0.05 °C.

The Li(20 μm)||LMO(0.1 mAh cm^{-2}) coin cells in LiTFSI–12C4@TTE/H_2O biphasic electrolytes show capacity retention of 91.1% of

https://doi.org/10.1038/s41565-025-01898-0

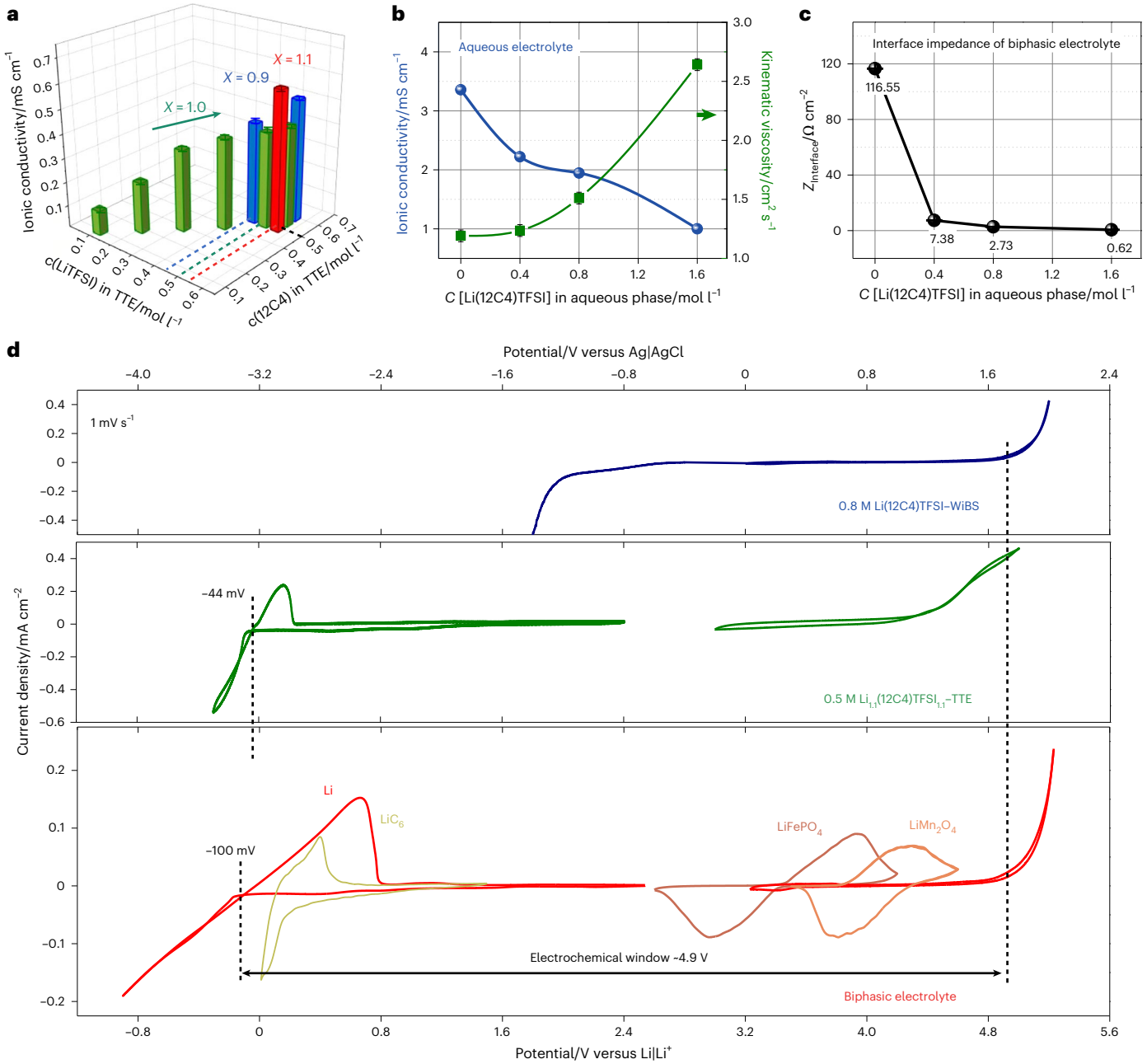

Fig. 3 | Electrochemical properties of biphasic electrolytes. a, The ionic conductivity of Li_x(12C4)$TFSI_x$–TTE organic electrolyte (25 ± 0.05 °C) for various LiTFSI salt and 12C4 concentrations, and LiTFSI:12C4 molar ratio *x*. Data are presented as average value ± standard deviation. **b**,**c**, The ionic conductivity and kinematic viscosity of the WiBS aqueous electrolyte (**b**) (25 ± 0.05 °C) and the interface impedance ($Z_{interface}$) of the biphasic electrolyte (**c**) with different concentrations of Li(12C4)TFSI complex added in the WiBS electrolyte. The interface impedance can be calculated by the equation shown in Supplementary Note 27. Data are presented as average value ± standard deviation. **d**, ESW of 0.8 M Li(12C4)TFSI–WiBS electrolyte measured with linear sweep voltammetry for the negative potential limit and CV for the positive potential limit. ESWs of 0.5 M $Li_{1.1}$(12C4)$TFSI_{1.1}$–TTE electrolyte and biphasic electrolytes measured with CV for both the negative and positive potential limits. All measurements were conducted at a scan rate of 1 mV s^{-1} and a temperature of 25 ± 0.05 °C. The CV measurements of LiC_6 (fully lithiated graphite), LFP and LMO electrodes were carried out in biphasic electrolytes at a scan rate of 1 mA s^{-1} with a high-mass-loading LFP electrode (1.5 mAh cm^{-2}, active materials 8.8 ± 0.1 mg cm^{-2}) or Li metal as the counter and reference electrode in biphasic or organic electrolyte, respectively, to balance the ions. The reductive and oxidative limits of the aqueous electrolyte are tested by using Ti and Al foils as working electrodes, respectively, with Ag|AgCl as a reference electrode. The reductive and oxidative limit potentials of $Li_{1.1}$(12C4)$TFSI_{1.1}$–TTE electrolyte and biphasic electrolyte were tested in a coin cell by using Cu and Al foil as working electrodes, respectively, with Li metal as a reference electrode. For convenience, the potential versus Ag|AgCl is converted to Li|Li^+ reference.

its initial capacity after 100 cycles (Fig. 4e,f) and 86.6% of its initial capacity after 1,200 cycles (Supplementary Fig. 34) with an average CE of 99.6% at 74 mA g^{-1} and 25 ± 0.05 °C. This performance is associated with the fast charge transfer rate of $Li^+(H_2O)(TFSI^-)$ involved in the LMO redox, while the minor amount of Li^+(12C4)($TFSI^-$) with low redox kinetic functions as support at the biphasic interface. The testing of a Li(20 μm)||LMO(0.1 mAh cm^{-2}) single-layer pouch cell with the LiTFSI–12C4@TTE/H_2O biphasic electrolyte (Fig. 4g) showed ~70% of discharge capacity retention after 500 cycles at 74 mA g^{-1} and 25 ± 0.05 °C. The increase in cycle performance shown in Fig. 4g and

https://doi.org/10.1038/s41565-025-01898-0

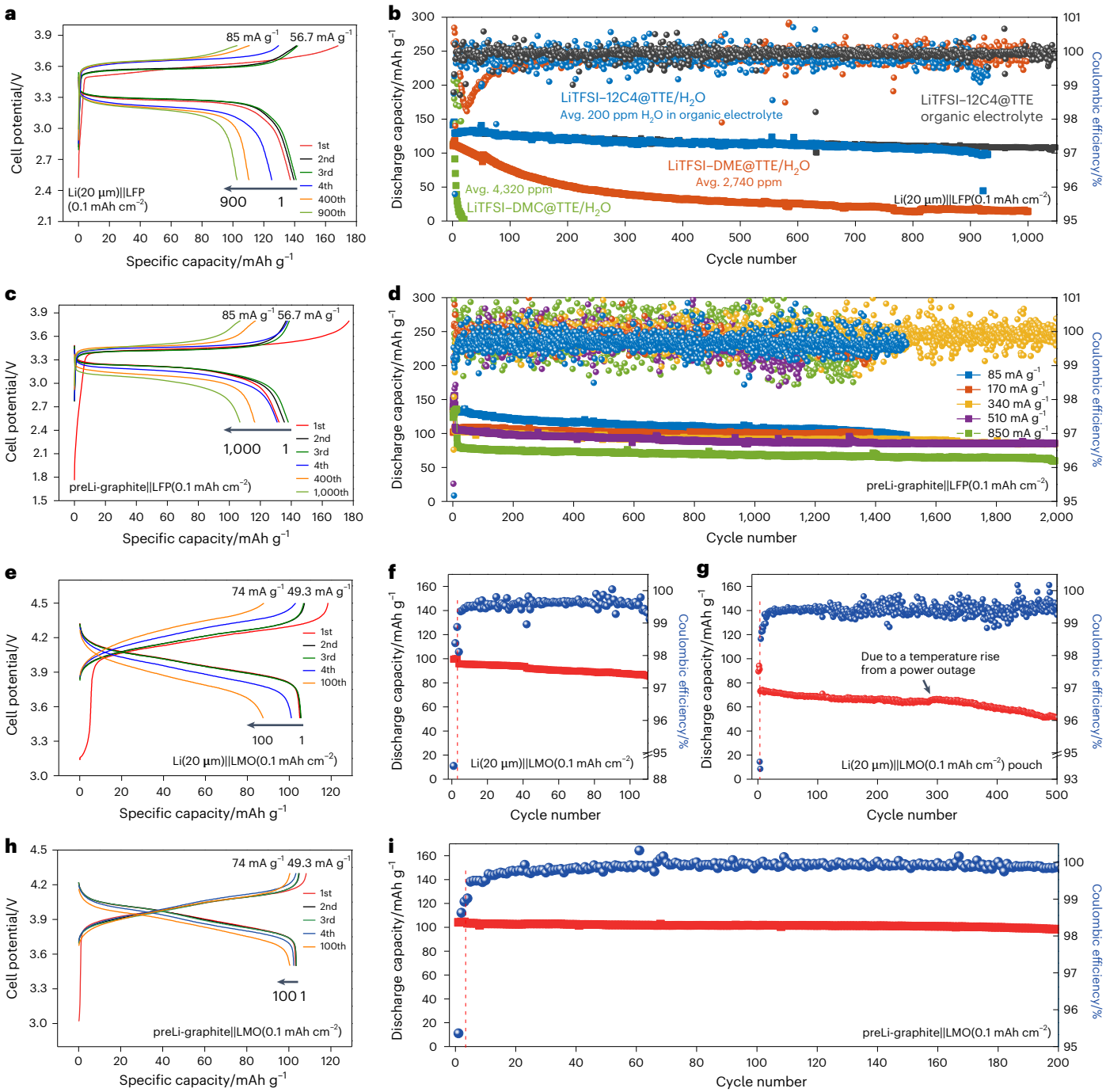

Fig. 4 | Testing of LiTFSI–12C4@TTE/H_2O biphasic electrolytes in various Li-based cell configurations. a, Galvanostatic charge–discharge (GCD) curves of Li(20 μm)||LFP coin cells in LiTFSI–12C4@TTE/H_2O biphasic electrolyte at a specific current of 85 mA g^{-1} (except for the first three cycles at a current of 56.7 mA g^{-1}). **b**, Cycling stability of Li(20 μm)||LFP coin cells in the LiTFSI–12C4@TTE/H_2O, LiTFSI–DME@TTE/H_2O and LiTFSI–DMC@TTE/H_2O biphasic electrolytes compared with the LiTFSI–12C4@TTE organic electrolyte at a specific current of 85 mA g^{-1} (except for the first three cycles at a current of 56.7 mA g^{-1}). **c**, GCD curves of prelithiated(preLi)-graphite||LFP coin cells in LiTFSI–12C4@TTE/H_2O biphasic electrolyte at 85 mA g^{-1} (except for the first three cycles). **d**, Cycling stability of preLi-graphite||LFP coin cells at 85 mA g^{-1}, 170 mA g^{-1}, 340 mA g^{-1}, 510 mA g^{-1} and 850 mA g^{-1}. **e**–**g**, GCD curves (**e**) and cycling stability (**f**) of Li(20 μm)||LMO coin cells, and Li(20 μm)||LMO single-layer pouch cell (**g**) in LiTFSI–12C4@TTE/H_2O biphasic electrolyte at 74 mA g^{-1} (except for the first three cycles). **h**,**i**, GCD curves (**h**) and cycling stability (**i**) of preLi-graphite||LMO coin cells at 74 mA g^{-1} (except for the first three cycles). All the cells were initially activated by applying a specific current of 56.7 mA g^{-1} for the first three cycles in cells with an LFP positive electrode and 49.3 mA g^{-1} for cells with an LMO positive electrode. The mass loading of LFP-based and LMO-based positive electrodes is 0.1 mAh cm^{-2}. All tests in this figure were conducted at 25 ± 0.05 °C. The applied potential range was 2.5–3.8 V for Li||LFP and preLi-graphite||LFP cells, 3.5–4.5 V for Li||LMO cells and 3.5–4.3 V for preLi-graphite||LMO cells.

Supplementary Fig. 34 is due to the temperature increase in the battery testing room after a power outage in the laboratory. Good cycle stability was also attained in preLi-graphite||LMO(0.1 mAh cm^{-2}) coin cells in LiTFSI–12C4@TTE/H_2O biphasic electrolytes (Fig. 4h,i) with 95.5% of the discharge capacity maintained after 200 cycles with an average CE of 99.9% at 74 mA g^{-1} and 25 ± 0.05 °C (Fig. 4i). Moreover, no

https://doi.org/10.1038/s41565-025-01898-0

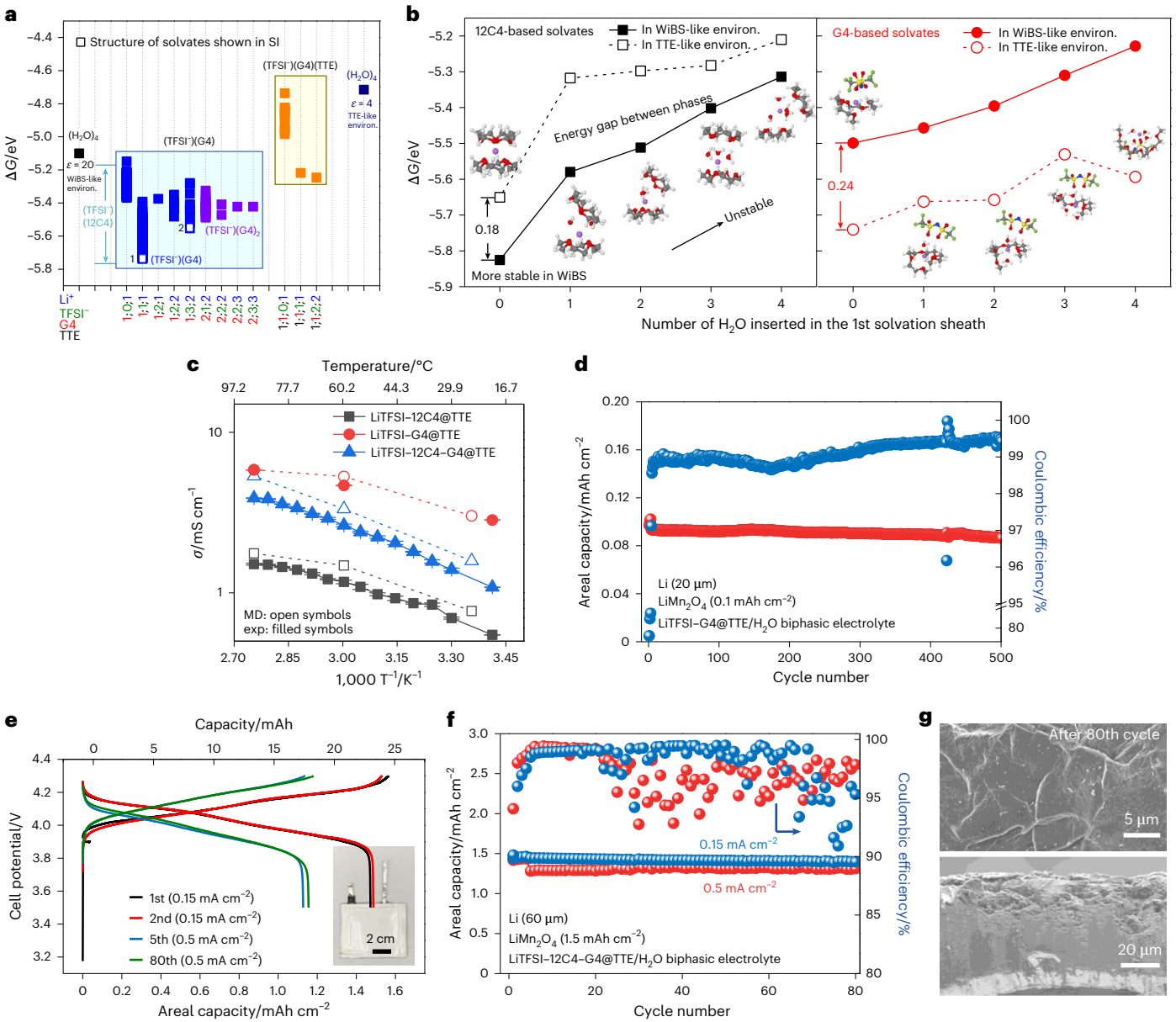

Fig. 5 | Generality at a practical value. a, Binding free energies (ΔG) of the $(TFSI^-)_a(Li^+)_b(G4)_c(TTE)_d$ solvates immersed in an implicit solvent (SMD(ether)) (Supplementary Note 8) relative to Li^+ in gas-phase and solvents/anions in implicit solvent. Solvates are highlighted by whether they contain G4 (blue region) or G4 in TTE (yellow region). The corresponding solvate binding energies (ΔE) and solvates (1–2) geometries are shown in Supplementary Fig. 43. **b**, The change in ΔG between Li^+ and the solvation shell as a function of the number of waters inserted into the Li^+ first solvation shell. Solvates are immersed in two different dielectric media corresponding to the organic phase (open symbols, dashed line) and WiBS phase (closed symbols, solid line). Insets are the corresponding geometries of the solvates. Atom colour legend in the insets: purple (Li); green (F); red (O); white (H); yellow (S); blue (N); and grey (C). **c**, Bulk ionic conductivity values of the non-aqueous electrolytes at various temperatures obtained via experimental measurements (data are presented as average value ± standard deviation) and MD simulations. **d**, Cycling stability of Li(20 μm)|LiTFSI–G4@TTE/H_2O|LMO (0.1 mAh cm^{-2}) single-layer pouch cells at a current of 0.05 mA cm^{-2} (except for the first three cycles at a current of 0.03 mA cm^{-2}) and a temperature of 25 ± 0.05 °C. **e**,**f**, Potential profiles (**e**) (photographic picture of the pouch cell in the inset) and cycling stability (**f**) of Li(60 μm)||LMO single-layer pouch cells with 1.5 mAh cm^{-2} areal mass loading using combined 12C4 + G4 ionophore in LiTFSI–12C4–G4@TTE/H_2O biphasic electrolyte at 0.15 mA cm^{-2} and 0.5 mA cm^{-2} (except for the first three cycles at a current of 0.15 mA cm^{-2}) and a temperature of 25 ± 0.05 °C. **g**, Magnified (upper) and cross-sectional (lower) ex situ SEM micrographs of the 60 μm Li metal electrode after 80 cycles in Li|LiTFSI–12C4–G4@TTE/H_2O|LMO single-layer pouch cells at 1.5 mAh cm^{-2}.

increases in potential hysteresis were observed in the potential profiles of these cells across different cycle numbers, indicating that the SEI and biphasic interfaces remain stable during cycling.

The physical properties and electrochemical performance of the biphasic electrolyte remain stable at temperatures up to 60 °C with an activation energy of 0.28 eV for the ionic conduction (Supplementary Note 16 and Supplementary Figs. 35 and 36). The Li(20 μm)|| Li(20 μm) symmetric cells with LiTFSI–12C4@TTE/H_2O biphasic electrolytes show a cycle life of more than 1,600 h at 45 ± 0.05 °C and 1,500 h at 60 ± 0.05 °C (Supplementary Fig. 37). At 45 ± 0.05 °C, the Li(20 μm)||LMO(0.1 mAh cm^{-2}) coin cell shows a discharge capacity retention of 98.0% of its initial discharge capacity after 100 cycles with an average CE of 99.7% at 74 mA g^{-1}. Increasing the temperature to 60 ± 0.05 °C, the Li(20 μm)||LMO(0.1 mAh cm^{-2}) cell still retains 98.2% of its initial discharge capacity after 100 cycles with an average CE of 99.6% at 74 mA g^{-1} (Supplementary Fig. 38).

Improvement of the biphasic electrolyte concept towards cost-effective and practical approaches for battery applications

The LiTFSI–12C4@TTE/H_2O biphasic electrolytes exhibit low flammability (Supplementary Fig. 39). However, the high cost and toxicity[23] of 12C4 and the amount of expensive LiTFSI salt required to prepare the electrolyte solution act as stumbling blocks for implementation in practical large-scale batteries.

To reduce the cost, the WiBS aqueous electrolyte was replaced either by WiS electrolyte solutions in the 5–21 m LiTFSI concentration range (Supplementary Fig. 40) or by a cost-effective 22 m $LiNO_3$ aqueous solution (Supplementary Fig. 41). Note that $LiNO_3$ is a highly energetic salt that may explode violently upon heating, shock, friction or impact[24]. Even in an aqueous solution, highly concentrated $LiNO_3$ poses severe safety risks when in contact with Li metal, even under an inert Ar atmosphere (Supplementary Fig. 41a,b). Despite these risks, Li(20 µm)||LFP(0.1 mAh cm^{-2}) and Li(20 µm)||LMO(0.1 mAh cm^{-2}) coin cells in $LiNO_3$–12C4@TTE/H_2O (where WIS aqueous electrolyte is 22 m $LiNO_3$ in H_2O) biphasic electrolytes demonstrate good cycling performance (Supplementary Fig. 41 and Supplementary Note 17). Other organic diluents such as 1,1,2,2-tetrafluoroethyl-2′,2′,2′-trifluoroethyl ether (HFE) also have a similar function as TTE (Supplementary Fig. 42).

The G4 solvent (US$135 kg^{-1}; Supplementary Table 2), with oxygen-aliphatic chains and a Li^+ binding motif similar to 12C4 (US$20,600 kg^{-1}; Supplementary Table 2) (Fig. 5a and Supplementary Fig. 43), serves as a viable alternative to 12C4. The 0.5 M $Li_{1.1}$(G4)$TFSI_{1.1}$–TTE/0.8 M Li(G4)TFSI–WiBS biphasic electrolyte (denoted as LiTFSI–G4@TTE/H_2O) exhibits a similar solvation structure in as observed in 12C4 systems (Supplementary Fig. 44 and Supplementary Note 18). In contrast, G4 has higher solubility in TTE and enables faster Li^+ desolvation than 12C4 (Supplementary Note 19). Moreover, Li^+(G4)-based solvates prefer the TTE environment over the WiBS environment (Fig. 5b) and exhibit higher bulk ionic conductivity from both MD simulations and experimental measurements (Fig. 5c) owing to the high fraction of Li^+(G4) SSIP (44%) (Supplementary Note 20). Li^+(G4) SSIPs exhibit a residence time two orders of magnitude longer than the faster-exchanging AGGs in the LiTFSI–12C4@TTE electrolyte (Supplementary Table 1), resulting in an interfacial impedance trend: Li^+(12C4) AGGs ≤ Li^+(G4) AGGs << $Li^+(H_2O)$ hydrates (Supplementary Note 21). Therefore, G4 functions similarly to 12C4 in biphasic electrolytes for Li metal coin cells (Supplementary Fig. 45 and Supplementary Note 22) and single-layer Li metal pouch cells (Fig. 5d and Supplementary Fig. 46) using LMO positive electrode with an areal capacity of 0.1 mAh cm^{-2}. However, the slow exchange of the Li^+(G4) species (Supplementary Fig. 47) limits the use of positive electrodes with an areal capacity of 1.5 mAh cm^{-2} (Supplementary Fig. 48).

Mixtures of G4 and 12C4 enhance salt solubility, increase charge carrier concentration and raise the Li^+:ionophore ratio x in the organic electrolyte from 1.1 to 1.5, making charged triple-ion nanocluster being a dominant species (Fig. 2c and Supplementary Note 23). These nanoclusters in the 1.5 M $Li(12C4)_{1/3}(G4)_{1/3}$TFSI–TTE organic electrolyte (denoted as LiTFSI–12C4–G4@TTE; Supplementary Fig. 49) contribute to both high bulk ionic transport of 1.1×10^{-3} S cm^{-1} at 25 ± 0.05 °C (Fig. 5c) and fast desolvation at the electrode|electrolyte interface owing to the relatively short Li^+–$TFSI^-$ residence times (Supplementary Table 1 and Supplementary Note 24) that enables the operation of positive electrodes with a practical areal capacity of 1.5 mAh cm^{-2} (~2.67 N/P) (Supplementary Figs. 50 and 51) at a temperature of 25 ± 0.05 °C.

The biphasic electrolytes with LiTFSI–12C4–G4@TTE organic phase and 0.8 M $Li(12C4)_{1/2}(G4)_{1/2}$TFSI–WIBS aqueous phase (denoted as LiTFSI–12C4–G4@TTE/H_2O) enable good rate performance and stable cycling of Li(20 µm)||LMO(1.5 mAh cm^{-2}) at 25 ± 0.05 °C (Supplementary Fig. 52) and even 45 ± 0.05 °C and 60 ± 0.05 °C (Supplementary Fig. 53). The 22.5 mAh Li(60 µm)|LiTFSI–12C4–G4@TTE/H_2O|LMO (1.5 mAh cm^{-2}) (~8 N/P) single-layer pouch cell retains 95.8% discharge capacity after 80 cycles at currents of 0.15 mA cm^{-2} and 0.5 mA cm^{-2} (except for the first three cycles at a current of 0.15 mA cm^{-2}) and a temperature of 25 ± 0.05 °C (Fig. 5e,f). After 80 cycles, the Li metal electrode collected from the Li|LiTFSI–12C4–G4@TTE/H_2O|LMO single-layer pouch cell shows a smooth surface (Supplementary Fig. 54) with no visible presence of dendrites (Fig. 5g). Cell pre-cycling (Supplementary Fig. 55a,b) and incorporating LiFSI in the non-aqueous phase of the biphasic electrolyte (Supplementary Fig. 55c,d) further enhance the average CE at a temperature of 25 ± 0.05 °C, reaching 99.01% for pouch cells with an N/P ratio of 4 at 0.5 mA cm^{-2}, and 99.46% for pouch cells with an N/P ratio of 1.6 at 1.5 mA cm^{-2}.

Moreover, the broad ESW of the biphasic electrolyte allows for the use of high-potential, high-capacity $LiVPO_4F$-based positive electrodes (Supplementary Fig. 56), validated with a commercially viable in situ prelithiation method (Supplementary Fig. 57 and Supplementary Note 25). The energy content of cells using the biphasic electrolyte was calculated based on state-of-the-art models reported in the literature[25,26]. When using a 25 µm thin Celgard 2500 separator (Supplementary Fig. 58) and considering all the other aspects of electrode and electrolyte (Supplementary Tables 3–7 and Supplementary Note 26), the projected specific energy and energy density values of the 18650-type Li|biphasic electrolyte|$LiVPO_4F$ cell are 284 Wh kg^{-1} and 651 Wh l^{-1}, respectively, slightly higher than the energy density (600–650 Wh l^{-1}) of commercial 18650 Li-ion cells[26]. The total cost of the Li-based batteries using the biphasic electrolyte system in this work can reach US$111.4 kWh^{-1} (Supplementary Table 8), estimated by the commercial battery model and the price of the biphasic electrolyte components (price for buying of kg-level quantities; Supplementary Table 2). Taking other factors (listed in Supplementary Table 8) into consideration, including cycle life, cell potential and safety, it is reasonable to expect that such chemistry could bridge the gap between commercial aqueous technologies, including lead-acid, Ni–MH batteries and state-of-the-art non-aqueous LIBs[5,27,28] (Supplementary Fig. 59).

Conclusion

In this work, we designed a 4.9 V biphasic electrolyte solution comprising two immiscible aqueous and non-aqueous phases containing lithium ionophore molecules such as 12C4 and/or G4 capable of suppressing water shuttling while minimizing interface impedance during Li^+ transport across the phase boundary. The LiTFSI–12C4@TTE/H_2O biphasic electrolyte tested in combination with graphite-based or Li metal negative electrodes and LFP- or LMO- based positive electrodes enable adequate cycle life with good discharge capacity and CE performance. By mixing the ionophores to formulate LiTFSI–12C4–G4@TTE/H_2O biphasic electrolyte solution and testing the latter in a 22.5 mAh Li||LMO single-layer pouch cell configuration with an areal capacity of 1.5 mAh cm^{-2}, we demonstrate a 95.8% discharge capacity after 80 cycles at areal currents of 0.15 mA cm^{-2} and 0.5 mA cm^{-2} (except for the first three cycles at a current of 0.15 mA cm^{-2}) and a temperature of 25 ± 0.05 °C. This study offers a strategy for the design of both hydrophobic and phase-separated electrolytes with beneficial properties for battery applications, which are not attainable with conventional single-phase electrolytes. The proposed biphasic electrolyte strategy requires further optimization in phase stability across all temperatures and long-term reliability to facilitate the transition of this strategy to commercial battery applications. We also envisage future research work on the use of the biphasic electrolyte design to limit moisture transfer to metal electrodes in metal–air batteries.

Online content

Any methods, additional references, Nature Portfolio reporting summaries, source data, extended data, supplementary information, acknowledgements, peer review information; details of author contributions and competing interests; and statements of data and code availability are available at https://doi.org/10.1038/s41565-025-01898-0.

References

1. Suo, L. et al. "Water-in-salt" electrolyte enables high-voltage aqueous lithium-ion chemistries. *Science* **350**, 938–943 (2015).
2. Xu, K. Electrolytes and interphases in Li-ion batteries and beyond. *Chem. Rev.* **114**, 11503–11618 (2014).
3. Xie, J., Liang, Z. & Lu, Y.-C. Molecular crowding electrolytes for high-voltage aqueous batteries. *Nat. Mater.* **19**, 1006–1011 (2020).
4. Cao, L. et al. Solvation structure design for aqueous Zn metal batteries. *J. Am. Chem. Soc.* **142**, 21404–21409 (2020).
5. Xu, J. et al. Aqueous electrolyte design for super-stable 2.5 V $LiMn_2O_4$ || $Li_4Ti_5O_{12}$ pouch cells. *Nat. Energy* **7**, 186–193 (2022).
6. Yang, C. et al. 4.0 V aqueous Li-ion batteries. *Joule* **1**, 122–132 (2017).
7. Li, H., Wang, Y., Na, H., Liu, H. & Zhou, H. Rechargeable Ni-Li battery integrated aqueous/nonaqueous system. *J. Am. Chem. Soc.* **131**, 15098–15099 (2009).
8. Wang, Y., He, P. & Zhou, H. A lithium–air capacitor–battery based on a hybrid electrolyte. *Energy Environ. Sci.* **4**, 4994–4999 (2011).
9. Bai, S., Liu, X., Zhu, K., Wu, S. & Zhou, H. Metal–organic framework-based separator for lithium–sulfur batteries. *Nat. Energy* **1**, 16094 (2016).
10. Qiao, Y. et al. Advanced hybrid electrolyte Li-O_2 battery realized by dual superlyophobic membrane. *Joule* **3**, 2986–3001 (2019).
11. Yang, S., Zhang, F., Ding, H., He, P. & Zhou, H. Lithium metal extraction from seawater. *Joule* **2**, 1648–1651 (2018).
12. Chao, D. & Qiao, S.-Z. Toward high-voltage aqueous batteries: super- or low-concentrated electrolyte? *Joule* **4**, 1846–1851 (2020).
13. Jackson, D. T. & Nelson, P. N. Preparation and properties of some ion selective membranes: a review. *J. Mol. Struct.* **1182**, 241–259 (2019).
14. Busche, M. R. et al. Dynamic formation of a solid-liquid electrolyte interphase and its consequences for hybrid-battery concepts. *Nat. Chem.* **8**, 426–434 (2016).
15. Scatena, L. F., Brown, M. G. & Richmond, G. L. Water at hydrophobic surfaces: weak hydrogen bonding and strong orientation effects. *Science* **292**, 908–912 (2001).
16. Benjamin, I. Recombination, dissociation, and transport of ion pairs across the liquid/liquid interface. Implications for phase transfer catalysis. *J. Phys. Chem. B* **117**, 4325–4331 (2013).
17. Volkov, A. G. in *Interfacial Catalysis* (ed. Volkov, A. G.) Ch. 1 (CRC Press, 2002).
18. Shirakawa, S. & Maruoka, K. Recent developments in asymmetric phase-transfer reactions. *Angew. Chem. Int. Ed.* **52**, 4312–4348 (2013).
19. Suo, L. et al. Advanced high-voltage aqueous lithium-ion battery enabled by "water-in-bisalt" electrolyte. *Angew. Chem. Int. Ed.* **128**, 7252–7257 (2016).
20. Fakhari, A. R. & Shamsipur, M. An NMR study of the stoichiometry and stability of lithium ion complexes with 12-crown-4, 15-crown-5 and 18-crown-6 in binary acetonitrile-nitrobenzene mixtures. *J. Incl. Phenom. Macrocycl. Chem.* **26**, 243–251 (1996).
21. Shamsipur, M. & Madrakian, T. Competitive NMR study of the complexation of some alkaline earth and transition metal ions with 12-crown-4, 15-crown-5 and benzo-15-crown-5 in acetonitrile solution using the lithium-7 nucleus as a probe. *J. Coord. Chem.* **52**, 139–149 (2000).
22. MacFarlane, D. R. et al. On the concept of ionicity in ionic liquids. *Phys. Chem. Chem. Phys.* **11**, 4962–4967 (2009).
23. Morrison, P. W. et al. Crown ethers: novel permeability enhancers for ocular drug delivery? *Mol. Pharm.* **14**, 3528–3538 (2017).
24. Gierczyk, B., Zalas, M. & Otłowski, T. High-energetic salts and metal complexes: comprehensive overview with a focus on use in homemade explosives (HME). *Molecules* **29**, 5588 (2024).
25. Betz, J. et al. Theoretical versus practical energy: a plea for more transparency in the energy calculation of different rechargeable battery systems. *Adv. Energy Mater.* **9**, 1803170 (2019).
26. Choi, J. W. & Aurbach, D. Promise and reality of post-lithium-ion batteries with high energy densities. *Nat. Rev. Mater.* **1**, 1–16 (2016).
27. Chao, D. et al. Roadmap for advanced aqueous batteries: from design of materials to applications. *Sci. Adv.* **6**, eaba4098 (2020).
28. Anuphappharadorn, S., Sukchai, S., Sirisamphanwong, C. & Ketjoy, N. Comparison the economic analysis of the battery between lithium-ion and lead-acid in PV stand-alone application. *Energy Procedia* **56**, 352–358 (2014).

[1]Department of Chemical and Biomolecular Engineering, University of Maryland, College Park, MD, USA. [2]Battery Science Branch, Energy Science Division, DEVCOM Army Research Laboratory, Adelphi, MD, USA. [3]Chemistry Division, Brookhaven National Laboratory, Upton, NY, USA. [4]Department of Materials Science and Engineering, University of Maryland, College Park, MD, USA. [5]Department of Chemistry and Biochemistry, University of Maryland, College Park, MD, USA. [6]Department of Physics and Atmospheric Science, Dalhousie University, Halifax, Nova Scotia, Canada.
✉e-mail: oleg.a.borodin.civ@army.mil; cswang@umd.edu

Methods

Materials for electrolyte preparation

1,1,2,2-Tetrafluoroethyl-2,2,3,3-tetrafluoropropylether (TTE, 99.5% purity, SynQuest Labs), 12C4 (98% purity, Sigma-Aldrich), tetraethylene glycol dimethyl ether (G4, ≥99% purity, Sigma-Aldrich), DMC (≥99% purity, Sigma-Aldrich), dimethoxyethane (DME, 99.5% purity, Sigma-Aldrich), 1,1,2,2-tetrafluoroethyl-2′,2′,2′-trifluoroethyl ether (HFE, 97% purity, SynQuest Labs) and fluoroethylene carbonate (FEC; 99.5% purity, <2 ppm H_2O, Gotion) were used after being dehydrated by molecular sieves with a 4 Å pore size. The water sequestration process was conducted in a glovebox under an Ar atmosphere at 25 ± 0.05 °C for 24 h, resulting in a final H_2O content of <2 ppm. Lithium bis(trifluoromethanesulfonyl)imide (LiTFSI; >98% purity, <2 ppm H_2O, Gotion), lithium trifluoromethanesulfonate (LiOTF; 99.9% purity, <2 ppm H_2O, Gotion), lithium bis(fluorosulfonyl)imide (LiFSI; 99.9% purity, <2 ppm H_2O, Gotion) and lithium hexafluorophosphate ($LiPF_6$; 99.99% purity, <2 ppm H_2O, Gotion) were directly used as received and lithium nitrate ($LiNO_3$; 99.99% purity, Sigma-Aldrich) was dissolved into mixed organic solvents in predetermined concentrations in a glovebox filled with argon with the H_2O and O_2 content <0.1 ppm and the average temperature inside the glovebox of 25 ± 0.05 °C. The electrolyte solutions were used for the cell assembly immediately after their preparation.

Preparation of the electrolyte solutions

The solubility method is used to screen electrolyte solutions. Specifically, the composition of the LiTFSI–12C4@TTE electrolyte is determined by preparing various electrolyte formulations and identifying the clear solution with the highest salt-to-ionophore ratio (x) (Supplementary Fig. 5). It is important to note that the electrolyte preparation order should be strictly followed: LiTFSI first, TTE second and 12C4 third. If the order is altered—such as by combining LiTFSI and 12C4 first—salt-12C4 aggregates are likely to form, which cannot dissolve into a clear electrolyte, even with heating.

The LiTFSI–12C4@TTE electrolytes were prepared by adding 0.5 M 12C4 and 0.55 M LiTFSI in TTE in an argon-filled glovebox at 25 °C. For the preparation of approximately 1 ml of the LiTFSI–12C4@TTE electrolyte, a 2 ml capped glass vial was used as the container. First, 157.90 mg of LiTFSI (0.55 M) was weighed, followed by the addition of 1 ml of TTE using a micropipette. Subsequently, 88.10 mg of 12C4 (0.5 M) was added using a 20–100 µl pipette. The vial was then capped and manually shaken at 25 °C for 30 s until the salt was completely dissolved, yielding a clear electrolyte solution. It is important to note that if the order of electrolyte preparation is altered—combine LiTFSI and 12C4 first—salt-12C4 aggregates are likely to form, which cannot be dissolved into a clear electrolyte even upon heating.

The LiTFSI–12C4@WiBS electrolytes were made by adding 0.8 M 12C4 and 0.8 M LiTFSI in the WiBS electrolytes in the fume hood in ambient air conditions. For the preparation of approximately 1 ml of electrolyte, a 2 ml capped glass vial was used as the container. First, 229.67 mg of LiTFSI (0.8 M) was weighed, followed by the addition of 1 ml of WiBS electrolyte using a micropipette. Subsequently, 140.96 mg of 12C4 (0.8 M) was added using a 20–100 µl pipette. The vial was then capped, and the solution was heated with a heat gun (Master; Model HG-801D) for 10 s, followed by vortex mixing using a Fisher vortex mixer (Vortex Genie 2; catalogue number 12-812) for 30 s. This heating and mixing process was repeated until the salt was completely dissolved, resulting in a clear electrolyte solution. It is important to note that if the order of electrolyte preparation is altered, causing the salt and 12C4 to mix first, salt-12C4 aggregates are likely to form. These aggregates cannot be dissolved into a clear electrolyte, even with heating.

The WiBS was prepared by adding 21 m LiTFSI and 7 m LiOTF in 1 g H_2O in the lab with the ambient air at 25 °C. In detail, 6.028 g LiTFSI and 1.092 g LiOTF were first added into the 20 ml glass vial. Later, 1 g of deionized water was added using a micropipette. The vial was then capped, and the solution was heated with a heat gun (Master; Model HG-801D) for 10 s, followed by vortex mixing using a Fisher vortex mixer (Vortex Genie 2; catalogue number 12-812) for 30 s. This heating and mixing process was repeated until the salt was completely dissolved, resulting in a clear electrolyte solution.

The LiTFSI–G4@TTE and LiTFSI–G4@WiBS electrolytes were prepared following the same procedure as for 12C4, with the only difference being the replacement of 12C4 with G4. In detail, 88.10 mg of 12C4 (0.5 M) in LiTFSI–12C4@TTE was substituted with 111.14 mg of G4 (0.5 M) and 140.96 mg of 12C4 (0.8 M) in LiTFSI–12C4@WiBS was substituted with 177.82 mg of G4 (0.8 M).

The LiTFSI–12C4–G4@TTE/H_2O biphasic electrolytes were prepared following the same procedure as for LiTFSI–12C4@TTE and LiTFSI–12C4@WiBS electrolytes mentioned above, with the only difference being the addition of G4 and LiTFSI salts. The non-aqueous organic electrolyte is made by adding 0.5 M 12C4, 0.5 M G4 and 1.5 M LiTFSI in TTE in an argon-filled glovebox at 25 °C. The aqueous electrolyte contains 0.8 M 12C4, 0.8 M G4 and 1.6 M LiTFSI in WiBS, and it is prepared in the fume hood in ambient air conditions. For the preparation of approximately 1.5 ml of the LiTFSI–12C4–G4@TTE electrolyte, a 2 ml capped glass vial was used as the container. First, 430.64 mg of LiTFSI (1.5 M) was weighed, followed by the addition of 1 ml of TTE using a micropipette. Subsequently, 88.10 mg of 12C4 (0.5 M) and 111.14 mg of G4 (0.5 M) were added using a 20–100 µl pipette. The vial was then capped and manually shaken at 25 °C for 30 s until the salt was completely dissolved, yielding a clear electrolyte solution. For the preparation of approximately 1 ml of LiTFSI–12C4–G4@H_2O electrolyte, a 2 ml capped glass vial was used as the container. First, 459.34 mg of LiTFSI (1.6 M) was weighed, followed by the addition of 1 ml of WiBS electrolyte using a micropipette. Subsequently, 140.96 mg of 12C4 (0.8 M) and 177.82 mg of G4 (0.8 M) were added using a 20–100 µl pipette. The vial was then capped, and the solution was heated with a heat gun (Master; Model HG-801D) for 10 s, followed by vortex mixing using a Fisher vortex mixer (Vortex Genie 2; catalogue number 12-812) for 30 s. This heating and mixing process was repeated until the salt was completely dissolved, resulting in a clear electrolyte solution. It is important to note that if the order of electrolyte preparation is altered, causing the salt and 12C4 to mix first, salt-12C4 aggregates are likely to form. These aggregates cannot be dissolved into a clear electrolyte, even with heating.

The LiTFSI–DMC@TTE/H_2O biphasic electrolyte was prepared following the same procedure as for LiTFSI–12C4@TTE and LiTFSI–12C4@WiBS electrolytes mentioned above, with the only difference being the addition of DMC rather than 12C4. In detail, the organic LiTFSI–DMC@TTE electrolyte is prepared by adding 0.55 M LiTFSI and 1 M (90.08 mg per 1 ml TTE) DMC in TTE in an argon-filled glovebox at 25 °C, while the LiTFSI–DMC@H_2O aqueous electrolyte was prepared by adding 0.8 M LiTFSI and 1.6 M DMC (144.128 mg DMC per 1 ml TTE) in WiBS electrolyte in the fume hood in ambient air conditions at 25 °C.

The LiTFSI–DME@TTE/H_2O biphasic electrolyte was prepared following the same procedure as for LiTFSI–12C4@TTE and LiTFSI–12C4@WiBS electrolytes mentioned above, with the only difference being the addition of DME rather than 12C4. In detail, the organic LiTFSI–DME@TTE electrolyte is prepared by adding 0.55 M LiTFSI and 2 M (360.48 mg per 1 ml TTE) DME in TTE in an argon-filled glovebox at 25 °C, while the LiTFSI–DME@H_2O aqueous electrolyte was prepared by adding 0.8 M LiTFSI and 3.2 M (576.77 mg per 1 ml TTE) DME within WiBS electrolyte in the fume hood in ambient air conditions at 25 °C.

The WiS electrolyte solutions in the 5–21 m LiTFSI concentration range were made by using 5 m, 10 m and 21 m LiTFSI in 1 g H_2O electrolyte in the lab under the ambient air at 25 °C. In detail, 1.435 g (5 m), 2.870 g (10 m) and 6.028 g (21 m) LiTFSI was first added into the 20 ml glass vial. Later, 1 g of deionized water was added using a micropipette. The vial was then capped, and the solution was heated with a heat gun (Master; Model HG-801D) for 10 s, followed by vortex mixing using

a Fisher vortex mixer (Vortex Genie 2; catalogue number 12-812) for 30 s. This heating and mixing process was repeated until the salt was completely dissolved, resulting in a clear electrolyte solution.

The LiTFSI–12C4@HFE/H_2O biphasic electrolytes were prepared in an argon-filled glovebox at 25 °C by adding 100 mg 12C4 and 162 mg LiTFSI in 5 g HFE in the 10 nl glass vial and manually shaken at 25 °C for 30 s until the salt was completely dissolved, yielding a clear electrolyte solution, as LiTFSI–12C4@HFE organic electrolyte, while the preparation method of aqueous LiTFSI–12C4@H_2O electrolytes remains unchanged as demonstrated above.

The $LiNO_3$–12C4@TTE/H_2O biphasic electrolytes were prepared following the same procedure as for LiTFSI–12C4@TTE and LiTFSI–12C4@WiS electrolytes mentioned above, with the only difference being the addition of $LiNO_3$ as salt instead of LiTFSI and the adjustment of concentration. The $LiNO_3$–12C4@TTE electrolytes were prepared by adding 0.05 mM 12C4 and 0.055 mM $LiNO_3$ in TTE in an argon-filled glovebox at 25 °C, then capped and manually shaken at 25 °C for 30 s until the salt was completely dissolved, yielding a clear electrolyte solution. The $LiNO_3$–12C4@WiS electrolytes were made by adding 0.05 mM 12C4 and 0.05 mM $LiNO_3$ in the 22 m $LiNO_3$ in H_2O electrolytes in the fume hood in ambient air conditions. For the preparation of approximately 1 ml of electrolyte, a 2 ml capped glass vial was used as the container. First, prepare a 22 m $LiNO_3$ in H_2O electrolyte by adding 1.516 g $LiNO_3$ to 1 g H_2O electrolyte under the ambient air at 25 °C in the lab. Then $LiNO_3$–12C4@WiS electrolytes were made by adding 0.05 mM 12C4 and 0.05 mM $LiNO_3$ in the 1 ml of 22 m $LiNO_3$ in H_2O electrolytes in a 2 ml glass vial. The vial was then capped, and the solution was heated with a heat gun (Master; Model HG-801D) for 10 s, followed by vortex mixing using a Fisher vortex mixer (Vortex Genie 2; catalogue number 12-812) for 30 s. This heating and mixing process was repeated until the salt was completely dissolved, resulting in a clear electrolyte solution. It is important to note that if the order of electrolyte preparation is altered, causing the salt and 12C4 to mix first, salt-12C4 aggregates are likely to form. These aggregates cannot be dissolved into a clear electrolyte, even with heating.

For the preparation of the LiFSI-enriched LiTFSI–12C4–G4@TTE/H_2O biphasic electrolyte used in the assembly and testing of high-loading pouch cells, a specific procedure was followed. In detail, the 0.5 M LiFSI was added into LiTFSI–12C4–G4@TTE as an organic part of the biphasic electrolyte in an argon-filled glovebox at 25 °C, while the preparation procedure of LiTFSI–12C4–G4@H_2O aqueous electrolyte remains unchanged as demonstrated above. For the preparation of approximately 1.5 ml of the LiFSI-enriched LiTFSI–12C4–G4@TTE electrolyte, a 2 ml capped glass vial was used as the container. First, 430.64 mg of LiTFSI (1.5 M) and 93.54 mg of LiFSI (0.5 M) were weighed, followed by the addition of 1 ml of TTE using a micropipette. Subsequently, 88.10 mg of 12C4 (0.5 M) and 111.14 mg of G4 (0.5 M) were added using a 20–100 µl pipette. The vial was then capped and manually shaken at 25 °C for 30 s until the salt was completely dissolved, yielding a clear electrolyte solution. It is important to note that if the order of electrolyte preparation is altered—combine salt and 12C4 first—salt-12C4 aggregates are likely to form, which cannot be dissolved into a clear electrolyte even upon heating.

Preparation of the polymeric gel electrolytes

To prevent cell failure caused by the aqueous phase coming into contact with the negative electrode owing to electrolyte flow during cell transportation and handling, the aqueous phase was gelled using a hydrophilic polymer[29,30] and one layer of separator (Whatman glass fibre GF/A unless otherwise specified) soaked with organic electrolyte was added to physically separate the negative electrode from the aqueous gel (Supplementary Fig. 23). The hydrophilic polymer electrolyte is prepared by ultraviolet (UV) curing the aqueous monomer precursor solution. Typically, the aqueous monomer precursor solutions were prepared by mechanically mixing 88 wt% poly(ethylene glycol) methyl ether (MPEGA, M_n = 480, Sigma-Aldrich) and 10 wt% 2-hydroxyethyl acrylate (96% purity, Sigma-Aldrich) monomers with the 2 wt% of poly(ethylene glycol)diacrylate (M_n = 700, Sigma-Aldrich) crosslinker using a magnetic stirrer in a glass vial. The mixing was performed in an air atmosphere at 25 °C for 5 min. Subsequently, 0.5 wt% of 2,2-dimethoxy-2-phenylacetophenone (99% purity, Sigma-Aldrich) photoinitiator was added and the solution was dissolved in a 20 ml amber glass vial in an air atmosphere at 25 °C. After adding the photoinitiator, the glass vial needs to be wrapped by the Al foil to prevent polymerization under indoor lighting. The aqueous electrolyte and monomer blends were then combined in a fixed 80:20 weight ratio in a 20 ml amber glass vial wrapped by Al foil and manually shaken for 30 s to obtain a clear solution. For electrochemical testing in a biphasic electrolyte, the aqueous electrolyte–monomer blends mixture was manually drop-cast onto electrodes, including the inner conductive part of the positive electrode cases (CR2032 for the coin cell) and inner conductive part of the positive tap (Al tap for the pouch cell), and placed under a Uvitron Intelliray 600 UV lamp with UVB bulbs (365 nm) and exposed for a total dose of 90 s.

Preparation of 1 M $LiPF_6$ in FEC electrolyte for the prelithiation process

The 1 M $LiPF_6$ in FEC electrolytes was prepared in an argon-filled glovebox at 25 °C. For the preparation of approximately 1 ml of the 1 M $LiPF_6$ in FEC electrolyte, a 2 ml capped glass vial was used as the container. First, 151.9 mg of LiTFSI (1 M) was weighed, followed by the addition of 1 ml of FEC using a micropipette. The vial was then capped and manually shaken at 25 °C for 30 s until the salt was completely dissolved, yielding a clear electrolyte solution. The electrolyte needs to be used immediately after preparation.

Electrode preparation and cell assembly

Electrode preparation. Li metal with a thickness of 20 µm, 40 µm and 60 µm (150 mm width × 10 m length, ≥99.9% purity, China Energy Lithium Company) on Cu foil (≥99.9% purity, 0.1 mm thickness) was directly used as negative electrodes.

The graphite-based electrodes were prepared by mixing (via Thinky mixer in an air atmosphere at 25 °C for 10 min) 80 wt% graphite active material (KS4, ≥99.4% purity, TIMCAL TIMREX, 2.4 µm average particle size), 10 wt% carbon black (Timcal Super C65, >99% purity, <50 nm primary particle size, Imerys) and 10 wt% polyvinylidene fluoride (≥99.4% purity, SAFT America) in *N*-methyl-2-pyrrolidone (<0.005% H_2O, 99.5%, Sigma-Aldrich) and then casting (under an air atmosphere at 25 °C) the slurry onto Cu foils (≥99.9% purity, 5 µm thickness, SAFT America) with a doctor blade and dried under vacuum at 80 °C for 12 h to remove the solvent before calendaring under a pressure of 100 MPa with a line speed of 1 meter per min. The graphite electrodes were cut into circular shapes with a diameter of 12 mm by a precision disc cutter (MSK-T-10, MTI), then weighed by an analytical balance (XSE105, Max 41 g/120 g = 0.01 mg/0.1 mg, Mettler Toledo) and vacuum-dried by a vacuum oven (AT09, Across International) at 80 °C for 12 h before transferring into the glovebox with an Ar atmosphere, where the H_2O and O_2 content were both maintained below 0.1 ppm. The average temperature inside the glovebox was 25 °C. The electrodes can be used immediately after transfer or stored for later use. Note that part of the available active Li is consumed to form the SEI at the graphite-based electrode|electrolyte interface during the initial charge/discharge cycles. A prelithiation step, in Li||graphite cell configuration using 1 M $LiPF_6$ in FEC electrolyte solution, is needed for this cell configuration to compensate for the loss of lithium inventory (Supplementary Fig. 33).

For the assembly of high-potential cells with the biphasic electrolytes, the graphite-based negative electrode was prelithiated to reduce the irreversible capacity loss. The direct-contacting prelithiation

method consists of putting in contact under an external pressure of 0.05 psi under an Ar atmosphere at 25 °C for 12 h a Li metal electrode (99.9% purity, MSE Supplies, 0.6-mm-thick × 12-mm-diameter round chip) and a graphite-based electrode (prepared using the method mentioned few lines above) using a 20 µl 1 M $LiPF_6$ in FEC electrolyte solution added between Li metal and graphite electrode as shown in Supplementary Fig. 33. The prelithiated graphite electrode was washed by combined solvents with a volume ratio of 12C4:TTE = 1:100 and vacuum-dried in the small chamber of the glovebox under an Ar atmosphere at 25 °C before cell assembly. The N/P ratio of the assembled coin cell is 1.5 ($Q_{\text{graphite before prelithiation}}/Q_{\text{positive electrode}} = 1.5$; Q represents the capacity).

Another prelithiation method used consists of putting in contact a thin Li foil (<5 µm, handmade by weighting 0.1–100 mg Li metal and pressing it into a foil using the bottom of a glass vial) to the back side of the Cu current collector of graphite-based electrodes (3.5 ± 1.5 µm graphite powders, China Steel Chemical). The N/P ratios of the assembled coin cell are 1.1, 1.2 and 1.4 before prelithiation ($Q_{\text{graphite before prelithiation}}/Q_{\text{positive electrode}} = 1.1$, 1.2 and 1.4). The actual N/P has been precisely controlled by adjusting the capacity of supplemented Li (calculated through the actual mass of Li × theoretical capacity), and then the actual N/P = $(Q_{\text{graphite before prelithiation}} + Q_{\text{lithium metal}})/Q_{\text{positive electrode}}$.

The high-mass-loading LFP positive electrodes (1.5 mAh cm^{-2}, 8.8 ± 0.1 mg cm^{-2} active material), LMO positive electrodes (1.5 mAh cm^2, 10.1 ± 0.1 mg cm^{-2} active material; 2.0 mAh cm^2, 13.3 ± 0.1 mg cm^{-2} active material; 2.5 mAh cm^2, 16.6 ± 0.1 mg cm^{-2} active material) and $LiVPO_4F$ positive electrodes (1.2 mAh cm^{-2}, 7.7 ± 0.1 mg cm^{-2} active material) were provided by SAFT America. Lateral dimensions of the electrode are 9 mm diameter circular shape for coin cells and 3 cm × 6 cm (for <2 mAh cm^2 positive electrode) and 3 cm × 4 cm (for >2 mAh cm^2 positive electrode) rectangular shape for pouch cells.

The low-mass-loading LFP (0.1 mAh cm^{-2}, 0.6 ± 0.01 mg cm^{-2} active material) and LMO (0.1 mAh cm^{-2}, 0.7 ± 0.01 mg cm^{-2} active material) positive electrodes were manually prepared in the lab by mixing (via Thinky mixer in an air atmosphere at 25 °C for 10 min) 80 wt% active material (LFP, >99% purity, 1.3–1.5% carbon coated on the surface, 1.5 µm average particle size, product number PO0127, MSE Supplies; or LMO, >99% purity, without carbon coating, product number PO0126, 14 µm average particle size, PO0126, MSE Supplies), 10 wt% carbon black (Timcal Super C65, >99% purity, <50 nm primary particle size, Imerys) and 10 wt% polyvinylidene fluoride (≥99.4% purity, SAFT America) in *N*-methyl-2-pyrrolidone (<0.005% H_2O, 99.5%, Sigma-Aldrich) and then casting (under an air atmosphere at 25 °C) the slurry onto Al foils (≥99.9% purity, 7.5 µm thickness, SAFT America) with a doctor blade and dried under vacuum at 80 °C for 12 h to remove the solvent before calendaring under a pressure of 100 MPa with a line speed of 1 meter per min. These positive electrodes were cut into circular shapes with a diameter of 12 mm by a precision disc cutter (MSK-T-10, MTI), and then weighed by an analytical balance (XSE105, Max 41 g/120 g = 0.01 mg/0.1 mg, Mettler Toledo), without further drying process. The electrodes were stored under an air atmosphere at 25 °C. The electrode can be either used immediately after preparation or stored in air at 25 °C for later use.

Cell assembly. For the assembly of CR2032 coin-type cells (stainless steel, MTI Corporation), the positive electrode is placed in the middle of the positive electrode case (that is, a case with a mesh texture, often referred to as the 'negative case' when purchased). A fixed volume (40 µl, using a 20–100 µl pipette) of the aqueous monomer precursor solution was filled onto the positive side of the cell covering the positive electrode and its case. This was followed by in situ gelation (air atmosphere, 25 °C) under a Uvitron Intelliray 600 UV lamp with UVB bulbs (365 nm) and with a total exposure time of the 90 s. As a result, the whole positive side of the cell is covered by the aqueous gel electrolyte to prevent contact and oxidization of the organic phase electrolyte at a high potential. The gelled positive side of the cell was transferred into the glovebox through an antechamber with 3 vacuum/argon purge cycles, and a fixed amount (40 µl, using a 20–100 µl pipette) of liquid organic electrolyte was filled in the cells. A piece of Whatman glass fibre GF/A (260 µm thickness, 16 mm lateral size, 1.6 µm average pore size, 60% porosity, 55% porosity, dried under vacuum at 80 °C for 12 h before cell assembly) or Celgard 2500 (25 µm thickness, 16 mm lateral size, 0.064 µm average pore size, dried under vacuum at 80 °C for 12 h before cell assembly) was added as a separator between the negative electrode and the gel-covered positive electrode to prevent the aqueous gel electrolyte from contacting the Li metal or graphite-based electrodes when crimping cells (MSK-110, MTI) to a pressure of 50 kg cm^{-2} during assembly, as shown in Supplementary Fig. 23.

For the assembly of single-layer pouch cells, one single-side positive electrode (3 cm × 6 cm for <2 mAh cm^2 positive electrode and 3 cm × 4 cm for >2 mAh cm^2 positive electrode), one single-side Li metal negative electrode (3.5 cm × 6.5 cm to match with <2 mAh cm^2 positive electrode and 3.5 cm × 4.5 cm to match with >2 mAh cm^2 positive electrode) and one layer of Whatman glass fibre GF/A separator (same size of the negative electrode) are used and the cell sealing (MTI, 3-in-1 Sealer, MSK-115-III, aluminium-laminated pouch bag, 10 s sealing) is carried out in a dry room (SAFT America, −40 °C dew point). Aluminium (99.99% purity, 0.1 × 5 × 30 mm, SAFT America) and nickel strips (99.99% purity, 0.1 × 4 × 61 mm, MTI) were attached by welding (MSK-800-2K, MTI) as electrode tabs to the sides of the positive and negative electrodes, respectively. To prevent the oxidation of the organic electrolyte at the positive electrode side, the positive strip inside the pouch was covered (simply paste the tape onto the strip) by Kapton film tape (S-11729, Uline). The positive electrode was covered by the aqueous gel, which was gelified via 90 s UVB bulbs (365 nm) exposure of 40 µl $cm^{-2}{}_{\text{positive el.}}$ liquid aqueous–monomer blends mixture. The 40 µl $cm^{-2}{}_{\text{positive el.}}$ liquid organic electrolyte was injected (using a 20–100 µl pipette) into the package, followed by sealing of the battery (MTI, 3-in-1 Sealer, MSK-115-III, aluminium-laminated pouch bag, 10 s sealing). The pouch cells were tested applying a stack pressure of 3 bar (BST-UBA5-VE, MTI). To allow ex situ morphology characterizations of Li metal electrodes after cycling in pouch cell configuration, an additional Celgard 2500 separator was added between the GF/A and Li metal to prevent the glass fibre separator from sticking to the lithium metal surface.

Electrochemical measurements

The linear sweep voltammetry measurements were carried out on a CHI660B electrochemical workstation for measuring the reduction potential limit of aqueous electrolytes at 25 ± 0.05 °C. The CV measurements were carried out on a CHI660B electrochemical workstation for measuring the oxidation potential limit of the aqueous electrolytes and the electrochemical window of the organic and biphasic electrolytes at 25 ± 0.05 °C. The ESW of aqueous electrolytes was measured using a Swagelok three-electrode cell with working electrodes at the two sides and reference electrode in the middle. The reduction and oxidation limit potentials of the aqueous electrolyte are tested by using Ti (99.7% purity, 0.032 mm thickness, Alfa Aesar) and Al foils (≥99.9% purity, 7.5 µm thickness, SAFT America) as working electrodes, respectively, with Ag|AgCl as a reference electrode. In detail, when testing the reduction limit potential, a Ti foil was used as the working electrode, while an Al foil served as the counter electrode. When testing the oxidation limit potential, an Al foil was used as the working electrode, while a Ti foil served as the counter electrode. The reduction and oxidation limit potentials of organic electrolytes and biphasic electrolytes were tested in a coin cell by using Cu (≥99.9% purity, 5 µm thickness, SAFT America) and Al foil as working electrodes, respectively, with Li metal as a reference electrode. In detail, when testing the reduction limit potential, a Cu foil was used as the working electrode, while an Al foil served as the counter electrode. When testing the oxidation limit potential, an

Al foil was used as the working electrode, while a Cu foil served as the counter electrode.

The CV measurements of graphite-based, LFP-based and LMO-based electrodes were measured in biphasic electrolytes using a coin cell at a scan rate of 1 mA s^{-1} with a partially delithiated high-mass-loading LFP electrode or Li metal as the counter and reference electrode to balance the ions. In detail, when testing the CV of negative electrode, the working electrode is the tested negative electrode in the organic phase, while the counter and reference electrode is the partially delithiated (to the plateau potential) LFP electrode in the aqueous phase. When testing the CV of positive electrode, the working electrode is the tested positive electrode in the aqueous phase, while the counter and reference electrode is the Li metal electrode in the organic phase.

Galvanostatic cycling tests were performed on a Landt (Landt CT2001A galvanostat) and Neware (Neware BTS4000 galvanostat) tester. Cycling conditions for each test are described in the discussion section or figure captions.

The mass of the specific current and specific capacity refers to the mass of the active material in the positive electrode. At least three cells were tested for a single electrochemical experiment to ensure reproducibility of the results.

The electrochemical impedance spectroscopy (EIS) measurements have been carried out using the Gamry Interface 1000 with the potentiostatic signal applied over the frequency range of 1,000,000–0.1 Hz, 10 data points per decade of frequency, 10 mV amplitude of the signal and 10 s open circuit potential time applied before carrying out the EIS measurements. Impedance spectra of three-electrode coin cells (Supplementary Fig. 48) were acquired over the frequency range of −1,000,000–0.01 Hz using coin cells that incorporate a small piece of lithium metal on Cu foil (select the edge part of the electrode and cut it into dimensions of 0.1 × 4 × 60 mm, with one end being lithium metal on Cu foil and the other end being Cu foil only without Li metal negative electrode) as the reference electrode in between the two layers of the separators with the Li metal side inside the cell and Cu side outside the cell (Supplementary Fig. 48). The ionic conductivities of the electrolyte solutions were measured carrying out EIS measurements in Pt||Pt blocking cells at various temperatures (275–343 K). The interface impedance of the biphasic electrolyte was measured using the sealed Pt||Pt blocking cells with 1 ml organic phase and 1 ml aqueous phase electrolytes added using 100–1,000 µl pipette. The cell impedance of the biphasic electrolytes was measured via EIS[31] by separately immersing two Pt electrodes (0.5 cm^2 area, 1 cm distance; Supplementary Fig. 15) with one in an organic 0.5 M $Li_{1.1}$(12C4)$TFSI_{1.1}$–TTE electrolyte and the other in aqueous WiBS electrolytes with *y* M of Li(12C4)TFSI. In detail, place the conductive pen (Pt||Pt blocking cells) horizontally in air atmosphere (Supplementary Fig. 15) under a constant ambient temperature (25 °C), ensuring that one Pt electrode is positioned on the top and the other on the bottom, with the biphasic interface located in the middle of the two Pt electrodes, and rest 12 h before the test. The interface impedance can be calculated by the equation shown in Supplementary Note 27. The activation energies E_a for the conduction were evaluated using the equation shown in Supplementary Note 28.

The electrochemical measurements were carried out in the environmental temperature at the range of 25 ± 0.05 °C. The electrochemical measurements within the temperature range of 20 ± 0.05 °C to 60 ± 0.05 °C were carried out in an environmental chamber (VWR Oven Gr Con 2.3CF).

Physicochemical characterization

The flammability tests were conducted by taking 1 ml of LiTFSI–12C4@TTE organic electrolyte soaked in a GF/A (260 µm thickness, 16 mm lateral size, 1.6 µm average pore size, 60% porosity, 55% porosity) separator and polymeric aqueous WiBS gel electrolytes made of 1 ml gel monomer blends. The experiment was performed in the fume hood in ambient air conditions and a constant ambient temperature (25 ± 0.05 °C). The electrolyte was ignited using a flame torch with butane gas for 5 s, and the burning time was observed and recorded. If no combustion occurred, it was classified as 'non-flammable'.

The water content in all non-aqueous electrolyte solutions before the formation of the biphasic electrolyte was determined with Karl Fischer titration and controlled to be under 10 ppm. In detail, the sample electrolytes are stored in a 5 ml glass vial sealed with a rubber septum (Precision Seal) under ambient air conditions at 25 °C. After the designated storage period, use a 1 ml syringe to extract 200 µl of the electrolyte, weighing the syringe before and after collection to determine the exact sample weight. Inject the collected electrolyte into the Karl Fischer titration apparatus, then read and record the water content value. For the biphasic electrolyte, any increases in water content of the non-aqueous organic phase result from H_2O crossover from the aqueous phase.

The kinematic viscosity of the various electrolyte solutions was measured using a Ubbelohde viscometer by placing it vertically in the air atmosphere and at a constant ambient temperature (25 °C). In detail, use suction to pull the liquid above the upper mark in the capillary, then release the suction to allow the electrolyte to flow naturally under gravity. Record the time taken for the meniscus to pass from the upper to the lower timing mark. Take at least three measurements and calculate the average for accuracy. Finally, the kinematic viscosity can be calculated by the equation shown in Supplementary Note 29.

Raman spectra were collected with a Horiba Jobin Yvon Labram Aramis using a 532 nm diode-pumped solid-state laser between 3,000 cm^{-1} and 100 cm^{-1}, with all the samples sealed in a test glass tube (air environment, 25 °C).

The NMR spectroscopy (Bruker AV NEO 400 MHz) was tested using a coaxial system. 12C4 was added to 0.55 M LiTFSI/TTE–acetonitrile(AN, 99.8% purity, anhydrous, Sigma-Aldrich)–H_2O(deionized, ≤4.3 µS cm^{-1}) (TTE:AN = 7:3 in weight, H_2O = 10,000 ppm) electrolytes (AN was used to improve the solubility of water in TTE for better analysis) with the molar ratio of the 12C4 to Li^+ increasing from 0 to 1.0 (meaning that the concentration of crown ether was in a range of 0–0.6 M) to study the stoichiometry of complexation. The C_6D_6 in the coaxial insert was used for the locking field. The aqueous electrolyte solutions were measured by using D_2O in the coaxial insert for the locking field.

The PDF characterization was performed at the 28-ID-2 beamline of the National Synchrotron Light Source II (NSLS II) of Brookhaven National Laboratory (BNL), using a photon wavelength of 0.18475 Å. The raw data were integrated using Fit2D software, followed by intensity correction, background removal, and Fourier transform in PDFgetx3 to obtain the PDF data.

Ex situ ^1H and ^{19}F NMR measurements of the electrolytes before and after cell cycling were performed using a 600 MHz liquid NMR spectrometer (Bruker AV III 600 MHz). To collect the electrolytes from the cycled cells, the cells were disassembled in an Ar-filled glovebox (25 °C) using a cell disassembling machine (MSK-110, MTI). Use clean stainless-steel tweezers to remove all solid materials from the battery casing and place them in a clean 20 ml glass vial. Using a 100–1,000 µl pipette, extract injecting 1.0 ml of vinylene carbonate (battery grade, 99.5% purity, acid <200 ppm, H_2O < 100 ppm) solvent in five steps (200 µl each) to rinse the inner surface of the positive and negative electrode casings. Collect the rinsing liquid into the same 20 ml glass vial containing the solid materials. Manually shake the vial, then let it stand for 5 min in the glovebox (Ar atmosphere, 25 °C). Use a syringe filter (hydrophobic PTFE, 25 mm, 0.45 µm, non-sterile, VWR North American) to extract the liquid, then use 100–1,000 µl pipette to collect 400 µl of extracted solution and mix with 400 µl of 0.1 M fluorobenzene (99% purity, Sigma-Aldrich) in DMSO-d_6 (99.9% purity, Cambridge Isotope Laboratories), and the final solution was sealed in the NMR tube (Wilmad) in the glovebox (Ar atmosphere, 25 °C) to make sure the sample has not been exposed to air (even for a very short period of time) and analysed by NMR (air, 25 °C). The residual molar amounts

were determined from the relative intensity of each component to the internal reference: DMSO-d_6 for 12C4, H-groups of TTE in the ^{1}H spectra, and fluorobenzene for $TFSI^-$ and F-groups of TTE in the ^{19}F spectra.

All the cycled samples were recovered from coin cells using the electrodes described above, cycled and washed by ionophore/TTE solvent, followed by characterizations of XPS and SEM (by a Hitachi SU-70 field emission scanning electron microscope). To collect the electrode from the cycled coin cells, the coin cells were stopped at the discharged state (the upper potential limit of Li||negative electrode coin cells and the lower potential limit of negative electrode||LFP coin cells) and disassembled in an Ar-filled glovebox (25 °C) using a cell disassembling machine (MSK-110, MTI). A clean stainless-steel tweezer was used to carefully remove the target electrode from the battery casing. The electrode surface was then washed with mixed solvents (12C4:TTE = 1:100 by volume) and subsequently vacuum-dried in the small chamber of the glovebox under an Ar atmosphere at 25 °C. The prepared electrode sample was affixed on the sample stage in an Ar-filled glovebox (25 °C). XPS experiments were carried out on high-resolution Kratos AXIS 165 X-ray photoelectron spectrometers using monochromic Al Ka radiation. To avoid exposure to air and moisture, samples were transferred from the glovebox to the XPS instrument directly using a sealed Lock&Lock box filled with Ar.

MD simulation methodology. MD simulations focused on the understanding of electrolyte structure and ion transport mechanism in the organic phase that consisted of 0.5 M $Li_{1.1}$(12C4)1.1 TFSI, 0.5 M $Li_{1.1}$(G4)$TFSI_{1.1}$ and 1.5 M Li(12C4)$_{1/3}$(G4)$_{1/3}$TFSI dissolved in TTE diluent corresponding to MD simulation cells containing 36 LiTFSI, 32 12C4 or G4 crown ether in 425 TTE for the single solvent (12C4 or G4) electrolyte and 90 LiTFSI, 30 12C4, 30 G4 in 400 TTE for the 12C4–G4 bi-solvent electrolyte with TTE diluent. A many-body polarizable force field APPLE&P[32] for LiTFSI, glyme and TTE was used[33,34], with one modification: the repulsion–dispersion parameters for fluorine in TTE were adjusted to match the density of 1,532 kg m^{-3} at 298 K from Murata et al.[35] and the experimentally measured[35] heat of vaporization of 40.2 kJ mol^{-1} at 308 K yielding a value of 40.6 kJ mol^{-1} at 298 K from 44.5 ns MD simulations of 512 TTE molecules. All force field parameters are given in the attached tar archive.

MD simulations predicted a TTE viscosity of 1.18 mPa s in good agreement with the experimentally measured 1.4 mPa s at 298 K. The TTE dihedral parameters were refit to reproduce QC energies for rotations around all dihedrals calculated at 10-degree steps using Møller–Plesset perturbation theory of second order (MP2) with aug-cc-pvTz basis at geometries from ωB97DX/aug-cc-pvTz DFT calculations. All quantum chemistry calculations were performed using Gaussian 16, Revision C.02 (ref. 36).

While the APPLE&P force field accurately predicted structural and transport properties of linear and cyclic ether-based electrolytes doped with LiTFSI[37–39], the force field has not been previously tested on crown ethers. Thus, we examined the ability of the APPLE&P force field to predict the distorted 12C4 lowest energy conformer geometry in a gas phase obtained from QC, G4MP2 and ωB97XD/6-31+G(d,p) DFT calculations and molecular mechanics (MM) using APPLE&P force field (FF) shown in Supplementary Fig. 6. This distortion is due to four intramolecular hydrogen bonds between ether oxygens and ethylene groups in 12C4, and it disappears upon the 12C4 binding to a Li^+ cation. Molecular mechanics calculations using a developed force field (MM(FF)) also confirmed the ability of the force field to predict the Li^+ binding energy to one crown ether with the same (a) and opposite (b) direction point to EO dipoles and two 12C4 crown ethers in good agreement with the composite QC, G4MP2 method as shown in Supplementary Fig. 6.

A dielectric constant (ε) of ether (4.24), as provided in the Gaussian QC software, was used to model the organic ether-containing phase. A dielectric constant of 20 was applied to model the concentrated electrolyte (WiBS), as it is known that the dielectric constant decreases from that of water (78) to 20 or lower with increasing salt concentration[40].

Ion self-diffusion coefficients, inverse van Hove ratio (ionicity) and viscosity were extracted following previously published methodology[41], as shown in Supplementary Note 11.

Binding free energy calculations. Binding free energies ΔG_b between Li^+ and the solvation shell were computed for solvates extracted from MD simulations using the monomer thermodynamic cycle as $\Delta G_b = \Delta G\left(Li_n^+ S_{i,m_i}\right) - n\Delta G\left(Li^+\right) - \sum_i m_i \Delta G(S_i)$. In this expression, $\Delta G\left(Li_n^+ S_{i,m_i}\right)$ is the free energy of the solvate, which may comprise one or more Li^+ and zero or more (m_i) of any of 12C4, G4, $TFSI^-$ or in some cases H_2O (species denoted by S_i). The middle term $n\Delta G\left(Li^+\right)$ is n times the free energy of isolated Li^+ in the gas phase and the final term is a sum over products of $m_i\Delta G(S_i)$, where m_i is the number of species S_i in the shell and $\Delta G(S_i)$ is the free energy of an isolated 12C4, G4 or $TFSI^-$ immersed in implicit solvent. In the cases considering solvation by water, we take $\Delta G(S_i)$ as the average free energy of a water molecule in the cage hexamer immersed in implicit solvent instead of a single water molecule in implicit solvent. This better represents the exchange of water between the solvation shell and bulk water. The binding free energy for cases involving water solvation closely aligns with single-ion hydration free energies of Li^+ predicted by Tissandier and later Kelly[42,43]. Calculations are performed at the SMD(ether, acetone (ε = 20), water)/ωB97XD/6-31+G(d,p) level of theory, except as noted for $n\Delta G\left(Li^+\right)$, which is in the gas phase[44,45]. All solvates were computed with SMD(ether), while only solvates of special interest were computed with SMD(acetone). The only free energy computed with SMD(water) is $Li^+(H_2O)_4$. The use of acetone instead of water for the other solvates of interest reflects the lower dielectric constant observed in WiS/WiBS electrolytes. We used Gaussian 16 rev C.02 for all DFT calculations[36]. To compute the free energies of isolated molecules, we also perform a conformer analysis using rdkit[46]. For simplicity, only the lowest energy conformer is considered in this analysis.

Inclusion and ethics

This study does not involve human participants, animal subjects or personally identifiable data.

Data availability

All relevant data that support the plots within this article and other findings of this study are available from the corresponding authors upon request. An Excel file containing an energy density calculator is available in supplementary materials.

Code availability

A tar archive containing the MD simulation set-up and a code for this paper is available in supplementary materials.

References

29. Logan, M. W. et al. UV-cured eutectic gel polymer electrolytes for safe and robust Li-ion batteries. *J. Am. Chem. Soc.* **8**, 8485–8495 (2020).
30. Zhang, J. et al. "Water-in-salt" polymer electrolyte for Li-ion batteries. *Energy Environ. Sci.* **13**, 2878–2887 (2020).
31. Meddings, N. et al. Application of electrochemical impedance spectroscopy to commercial Li-ion cells: a review. *J. Power Sources* **480**, 228742 (2020).
32. Borodin, O. Polarizable force field development and molecular dynamics simulations of ionic liquids. *J. Phys. Chem. B* **113**, 11463–11478 (2009).
33. Borodin, O. et al. Insights into the structure and transport of the lithium, sodium, magnesium, and zinc bis(trifluoromethanesulfonyl)imide salts in ionic liquids. *J. Phys. Chem. C.* **122**, 20108–20121 (2018).

34. Glaser, R., Borodin, O., Johnson, B., Jhulki, S. & Yushin, G. Minimizing long-chain polysulfide formation in Li-S batteries by using localized low concentration highly fluorinated electrolytes. *J. Electrochem. Soc.* **168**, 090543 (2021).
35. Murata, J. et al. Vapor pressures of hydrofluoroethers. *J. Chem. Eng. Data* **47**, 911–915 (2002).
36. Gaussian 16 Rev. C.01. (Gaussian, 2016).
37. Alvarado, J. et al. Bisalt ether electrolytes: a pathway towards lithium metal batteries with Ni-rich cathodes. *Energy Environ. Sci.* **12**, 780–794 (2019).
38. Yang, Y. et al. High-efficiency lithium-metal anode enabled by liquefied gas electrolytes. *Joule* **3**, 1986–2000 (2019).
39. Steinrück, H.-G. et al. Concentration and velocity profiles in a polymeric lithium-ion battery electrolyte. *Energy Environ. Sci.* **13**, 4312–4321 (2020).
40. Nakayama, Y. Nonlinear dielectric decrement of electrolyte solutions: an effective medium approach. *J. Colloid Interface Sci.* **646**, 354–360 (2023).
41. Borodin, O. & Smith, G. D. Quantum chemistry and molecular dynamics simulation study of dimethyl carbonate: ethylene carbonate electrolytes doped with LiPF6. *J. Phys. Chem. B* **113**, 1763–1776 (2009).
42. Tissandier, M. D. et al. The proton's absolute aqueous enthalpy and Gibbs free energy of solvation from cluster-ion solvation data. *J. Phys. Chem. A* **102**, 7787–7794 (1998).
43. Kelly, C. P., Cramer, C. J. & Truhlar, D. G. Aqueous solvation free energies of ions and ion–water clusters based on an accurate value for the absolute aqueous solvation free energy of the proton. *J. Phys. Chem. B* **110**, 16066–16081 (2006).
44. Marenich, A. V., Cramer, C. J. & Truhlar, D. G. Universal solvation model based on solute electron density and on a continuum model of the solvent defined by the bulk dielectric constant and atomic surface tensions. *J. Phys. Chem. B* **113**, 6378–6396 (2009).
45. Chai, J.-D. & Head-Gordon, M. Long-range corrected hybrid density functionals with damped atom–atom dispersion corrections. *Phys. Chem. Chem. Phys.* **10**, 6615–6620 (2008).
46. Greg, L., Paolo, T., and Brian, K. rdkit/rdkit: 2022_09_3 (Q3 2022) Release (Release_2022_09_3). *Zenodo* https://zenodo.org/record/7415128 (2022).

Acknowledgements

This work is supported by the Aqueous Battery Consortium, an energy innovation hub under the US Department of Energy, Office of Basic Energy Sciences, Division of Materials Science and Engineering (O.B. and C.W.), the US Department of Energy ARPA-E Grant DEAR0000389, DEVCOM Army Research Laboratory under a cooperative agreement number W911NF-20-2-0284 (O.B. and C.W.). The work done at BNL is supported by the Assistant Secretary for Energy Efficiency and Renewable Energy (EERE), Vehicle Technology Office (VTO) of the US Department of Energy (DOE) through the Advanced Battery Materials Research (BMR) Program under contract number DE-SC0012704 (E.H., S.T. and X.-Q.Y.). This research used the 28-ID-2 (XPD) beamline of the National Synchrotron Light Source II, US DOE Office of Science User Facilities operated for the DOE Office of Science by BNL under contract number DE-SC0012704.

Author contributions

X.Z., C.Y. and C.W. proposed the research and designed the experiments. X.Z., N.Z., J.X., A.L.P. and W.Z. prepared the materials and performed the electrochemical experiments. S.T., E.H. and X.-Q.Y. conducted the PDF experiments. T.P.P. and O.B. conducted the QC calculations and MD simulations. X.Z. and F.C. carried out the NMR analysis. X.Z. and Y.L. carried out the SEM analysis. All the authors discussed the results, analysed the data and drafted the paper.

Competing interests

The authors declare no competing interests.

Additional information

Supplementary information The online version contains supplementary material available at https://doi.org/10.1038/s41565-025-01898-0.

Correspondence and requests for materials should be addressed to Oleg Borodin or Chunsheng Wang.

Peer review information *Nature Nanotechnology* thanks the anonymous reviewers for their contribution to the peer review of this work.